FEATURE ARTICLE

Check for updates

Recent progress on MN$_4$ macrocycle-derived oxygen reduction reaction electrocatalysts for polymer electrolyte fuel cell applications

Zubair Ahmed, [ID] [a] Karina Muñoz-Becerra, [ID] *[b] Srinu Akula, [ID] [a] José H. Zagal*[c] and Kaido Tammeveski [ID] *[a]

Transportation and power generation sectors have been garnering strong support for fuel cell-based technologies in recent times for emission-free energy conversion. However, the performance of these devices largely relies on the costly and scarce Pt-group metal-based electrocatalysts, which hinder their widespread commercialization. For the past few decades, vast research efforts have been focused on cost-effective and efficient non-precious metal electrocatalysts for low-temperature fuel cells. Single-atom catalysts (SACs) have attracted the most attention due to their excellent electrocatalytic performance. Moreover, SACs derived from transition metal MN$_4$ macrocycles have many advantages in terms of the structural integrity of the active centers that are beneficial for superior electrocatalytic activity and durability. This feature article covers recent reports focused on the development of MN$_4$ macrocycle-derived oxygen reduction reaction (ORR) electrocatalysts for proton exchange membrane fuel cells (PEMFCs) and anion exchange membrane fuel cells (AEMFCs), and summarizes the viability in energy applications, including their stability issues. This review aims to discuss the various factors that influence the fuel cell performance of cathode catalysts based on transition-metal macrocyclic complexes (metal porphyrins and phthalocyanines).

[a] *Institute of Chemistry, University of Tartu, Ravila 14a, 50411 Tartu, Estonia. E-mail: kaido.tammeveski@ut.ee; Tel: +372 7375168*

[b] *Centro Integrativo de Biología y Química Aplicada (CIBQA), Facultad de Ciencias de la Salud, Universidad Bernardo O'Higgins, General Gana 1702, Región Metropolitana, Santiago, 8370854, Chile. E-mail: karina.munoz@ubo.cl; Tel: +562 24772204*

[c] *Laboratorio de Electrocatálisis y Electrónica Molecular, Departamento de Química de los Materiales, Facultad de Química y Biología, Universidad de Santiago de Chile, Av. Libertador Bernardo O'Higgins 3363, Estación Central, Santiago 9170124, Chile. E-mail: jose.zagal@usach.cl; Tel: +562 27181075*

Zubair Ahmed finished his MSc in 2014 from Jamia Millia Islamia, New Delhi. After this, he completed his PhD thesis at the Institute of Nano Science and Technology (INST), Mohali, India, in 2022. He then joined the Institute of Chemistry at the University of Tartu, Estonia in 2022 as a post-doctoral fellow working with Professor Kaido Tammeveski. Currently, he is an MSCA postdoctoral fellow at Sorbonne University, France. His research focuses on developing original nanostructured materials for electrocatalytic applications.

Zubair Ahmed

Karina Muñoz-Becerra, Industrial Chemist, is the Director of the PhD Program in Science with a Mention in Functional Materials at Universidad Bernardo O'Higgins (UBO), Chile and an Associate Professor at the Integrative Center for Biology and Applied Chemistry (CIBQA-UBO). She received her PhD in Chemistry from Universidad de Santiago de Chile in 2015, where she was distinguished as the Best Doctoral Student. From 2015 to 2021, she carried out postdoctoral research in inorganic and applied electrochemistry. Her research focuses on the experimental design and DFT calculation-based theoretical studies of coordination-based and M–N–C single-atom carbon-derived transition-metal electrocatalysts for green hydrogen production and utilization.

Karina Muñoz-Becerra

1. Introduction

Polymer electrolyte fuel cells are economically viable and sustainable electrochemical energy conversion devices that have received increasing attention during the last decade.[1,2]
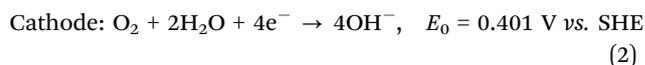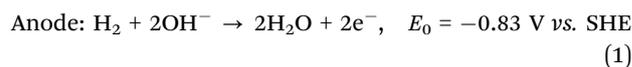
Srinu Akula was born in Vizianagaram (India) in 1989. He graduated from Pondicherry University (India) in 2013 and was awarded a PhD degree in 2020 at the Academy of Scientific and Innovative Research and CSIR-Central Electrochemical Research Institute-Madras Unit, where he worked on several R&D projects involving PEMFCs. During 2021–2023, he was a Postdoctoral Fellow at the Institute of Chemistry of the University of Tartu, working with Prof. Kaido Tammeveski. Since 2023 he has been a Research Associate at the Institute of Chemistry of the University of Tartu. His research is focused on the design of novel non-precious metal-based electrocatalysts for low temperature fuel cells. He is a co-author of more than 33 original articles and reviews. In 2026, he received the Estonian National Science Award.

Anion exchange membrane fuel cells (AEMFCs) and proton exchange membrane fuel cells (PEMFCs) consist of an anode and a cathode coated with catalyst layers on a gas diffusion layer (GDL) electrode and with an ion exchange membrane. In AEMFCs, O_2 is reduced in the presence of water to OH^- ions at the cathode that migrate through the anion exchange membrane (AEM) to the anode side, reacting with H_2 to produce H_2O as the final product (reactions (1)–(3)).[3] During these processes, electrons that are generated at the anode are collected by current collectors and transferred to the cathode electrode through the external circuits. The ideal AEMs must have excellent OH^- conductivity and ion exchange capacity, chemical and thermal stabilities, mechanical strength, flexibility, and low gas permeability, while preventing fuel crossover and a circuit break by blocking the electron transport through it.[3] The theoretical thermodynamic cell voltage of a single AEMFC is 1.23 V at room temperature. However, the practical cell voltage is much less than 1.23 V due to the cathodic and anodic overpotentials, ohmic drop, mass-transport losses, and fuel crossover. Hydrogen-fueled AEMFCs:

$$\text{Anode: } H_2 + 2OH^- \rightarrow 2H_2O + 2e^-, \quad E_0 = -0.83 \text{ V } vs. \text{ SHE} \tag{1}$$

$$\text{Cathode: } O_2 + 2H_2O + 4e^- \rightarrow 4OH^-, \quad E_0 = 0.401 \text{ V } vs. \text{ SHE} \tag{2}$$

$$\text{Overall reaction: } O_2 + 2H_2 \rightarrow 2H_2O, \quad E_0 = 1.23 \text{ V} \tag{3}$$

PEMFCs share many technical similarities with AEMFCs. The main difference lies in the type of ion exchange membrane

José H. Zagal

José Heráclito Zagal is a Distinguished & Emeritus Professor in the Faculty of Chemistry and Biology at the University of Santiago de Chile, and graduated from the University of Chile in 1973. He achieved his PhD from Case Western Reserve University, USA (1978) and was a Postdoc in Brookhaven National Laboratory in 1982. He has received several distinctions, the most important: Honorary Diploma, Global Energy Association (Russia), 2025, National Prize for Natural Sciences, 2024 (Chile), and the Presidential Chair of Science (1996, Chile). He is a Fellow of the Royal Society of Chemistry, the International Society of Electrochemistry, and a Fellow and elected Emeritus Member of the Electrochemical Society. He received the ''Agustin Arévalo'' Award from the Ibero-American Society of Electrochemistry in 2018. His fields of study are electrocatalysis and molecular electrochemistry and he has published more than 260 scientific articles, 8 book chapters, 7 books and 3 patents. He is well known for his development of reactivity descriptors for molecular catalysts in electrochemistry.

Kaido Tammeveski

Kaido Tammeveski was born in Tartu (Estonia) in 1964. In 1989, he graduated from the University of Tartu as a Chemist. He was awarded a PhD degree in 1998 at the same university. During 1999–2000, he was a Postdoctoral Fellow at the University of Liverpool (UK) working with Professor David J. Schiffrin. He has been the Head of the Chair of Colloid and Environmental Chemistry at the University of Tartu since 2001. He has been a Professor of Colloid and Environmental Chemistry at the Institute of Chemistry at the University of Tartu since 2021. His main research interest is oxygen reduction electrocatalysis and he is also involved in fuel cell and zinc–air battery research. He has published more than 260 scientific articles and has supervised the completion of 16 PhD theses. In 2014 and 2026, he received the National Science Award.

used in each system. However, as protons diffuse much faster than OH^- ions and as a result, PEMFC manages to obtain higher ionic conductivity and power density. Anodic and cathodic reactions in the PEMFC with H_2 gas as a fuel are given in reactions (4)–(6):

$$\text{Anode: } H_2 \rightarrow 2H^+ + 2e^-, \quad E_0 = 0 \text{ V } vs. \text{ SHE} \quad (4)$$

$$\text{Cathode: } O_2 + 4H^+ + 4e^- \rightarrow 2H_2O, \quad E_0 = 1.23 \text{ V } vs. \text{ SHE} \quad (5)$$

$$\text{Overall reaction: } 2H_2 + O_2 \rightarrow 2H_2O, \quad E_0 = 1.23 \text{ V} \quad (6)$$

The oxygen reduction reaction (ORR) process may follow two main pathways in aqueous media. The desired $4e^-$ ORR pathway involving the splitting of the O–O bond shows a minimum yield of peroxide formation.[4] In contrast, in a $2e^-$ ORR pathway, a high peroxide yield is involved, which is detrimental to the fuel cell catalyst and membrane stability.[5–7] It is not only detrimental to the fuel cell components, but the peroxide route delivers much less energy as compared to the full 4-electron reduction pathway. A well-established methodology is available to obtain ORR kinetic parameters from the rotating (ring)-disk electrode (RRDE/RDE) tests. However, due to several aspects such as a thin layer of catalyst in the RDE/RRDE test applied to a glassy carbon electrode instead of a gas diffusion layer, differences in gas flow pattern, water flooding at micropores, *etc.*, the experimental results in the RDE/RRDE system might mismatch the environment of polymer electrolyte fuel cells.[8–17]

Platinum group metal-based electrocatalysts are mainly used at the polymer electrolyte fuel cell anode, the cathode, or both.[18,19] Importantly, non-precious metal catalysts have been considered for years as low-cost promising alternatives, especially at the cathode electrode.[20,21] In particular, transition-metal–nitrogen–carbon (M–N–C) type ORR electrocatalysts have received an increased attention during the last two decades.[20,21] There is a large amount of literature dealing with metal macrocyclic complexes (metalloporphyrins, metallophthalocyanines, metallocorroles) for ORR applications,[22–29] however, there are only a few reviews concentrating on their fuel cell performance.[30–32] This review focuses on the rational design for the development of highly efficient transition metal MN_4 macrocycle-based ORR electrocatalysts to boost their performance in AEMFC and PEMFC applications.

2. ORRs on transition metal macrocycle-derived M–N–C catalysts

Despite their excellent ORR activity, MN_4 macrocycles face important limitations, especially in acidic media, where metal center dissolution and degradation of the macrocyclic framework compromise their stability and long-term durability. Furthermore, their inherently low electrical conductivity restricts charge transport, thereby limiting overall electrocatalytic performance. To address these issues, various strategies have been developed to immobilize MN_4 macrocycles onto conductive carbon supports. These include simple physical adsorption through π–π stacking interactions and covalent or

coordinative attachment *via* axial ligands such as pyridine.[33–35] The physicochemical properties of the carbon support – particularly, specific surface area, porosity, and electrical conductivity – play a crucial role in determining the electrocatalytic performance of the resulting catalyst materials. These parameters have been extensively investigated for both pristine MN_4 macrocycles supported on nanostructured carbons and their corresponding pyrolyzed M–N–C derivatives. In particular, high surface area and well-developed porosity enhance the accessibility and dispersion of active sites, leading to improved electrocatalytic ORR activity.[33,34,36] A notable example involves single-walled carbon nanotubes functionalized with pyridine moieties, which were employed as axial ligands for pristine (16Cl)FePc complexes. This strategy led to improved ORR performance in alkaline media, attributed to electronic interactions between the macrocycle and the functionalized support, which modulate the electronic density and 3d-orbital configuration of the Fe-center in the FeN_4 core, thereby optimizing adsorption of oxygenated intermediates.[34] Such electronic perturbations resemble those observed in pyrolyzed M–N–C catalysts. In these systems, the N-doped carbon matrix acts not only as a support but also as an electronic modulator of the anchored MN_4 sites, which is fundamental to their enhanced ORR activity. Fe phthalocyanine (FePc) and Co porphyrin physically adsorbed on the reduced graphene oxide (rGO) nanosheets exhibited excellent electrocatalytic activity for ORRs in alkaline media. This indicates efficient electron transfer between intact MN_4 macrocycles and rGO, and, therefore, these catalyst materials are very promising for ORR applications.[37] A recent study by Zhao *et al.*[38] employing a model Fe–N–C catalyst based on a conjugated FePc=FePc dimeric system supported on carbon black XC-72 provided important insights into the nature of the ORR-active sites. The authors proposed that the primary ORR-active site corresponds to a five-coordinated OH-$Fe^{3+}N_4$ moiety with a spin multiplicity of 5/2, in which all five Fe 3d-orbitals are singly occupied. Density functional theory (DFT) calculations demonstrated that a moderate d–π interaction between the Fe center and the conjugated carbon plane governs both the spin-state of the active centers and their adsorption energies with the oxygenated reaction intermediates, ultimately accounting for their superior ORR activity. The integration of MN_4 macrocyclic complexes with carbon substrates induces electronic modulation at the active site through intermolecular charge transfer. DFT calculations suggest that the highest occupied molecular orbital of the MN_4 complex in MN_4 macrocycle-carbon composites aligns favorably with the π* orbital of O_2, thereby promoting oxygen activation and reduction.[34,39] Although these supported macrocycles serve as valuable model systems for fundamental mechanistic studies in ORR electrocatalysis, their practical application remains constrained by insufficient activity and stability under operando conditions.[9,38,40] A mechanistic study by Wan *et al.*[41] provided important insights into the degradation pathway of FePc supported on KJ600 carbon black. Under acidic, O_2-saturated electrolyte at applied potentials, the reactive oxygen species, particularly $^\bullet OH$ and $^\bullet OOH$ radicals, were identified as

the main contributors to degradation. These species initiate hydroxylation at the C=C bonds within the macrocycle, disrupting aromaticity, breaking C–N bonds, and ultimately leading to demetallation of the Fe center.

2.1. Thermal conversion of MN₄-macrocycles for obtaining M–N–C catalysts

Following Jasinski's pioneering report on Co phthalocyanine as an ORR catalyst,[42] Jahnke and co-workers demonstrated that pyrolyzing MN_4 complexes supported on carbon under an inert atmosphere significantly improved both activity and stability in acidic media compared to their unpyrolyzed counterparts.[43,44] This pivotal study laid the groundwork for developing pyrolyzed M–N–C catalysts, utilizing MN_4 macrocycles and other metal, nitrogen, and carbon precursors as starting materials.[45–48] The thermal conversion of MN_4 macrocycles typically involves first supporting the pristine complex on a conductive, high-surface-area carbon matrix, such as carbon black[47–51] or carbide-derived carbons (CDC),[52] followed by pyrolysis at 400–1000 °C under inert or NH_3 atmospheres. The thermal treatment methodology used to obtain pyrolyzed M–N–C catalysts is a critical factor in determining their electrocatalytic activity. In many cases, a post-pyrolysis acid washing step is applied to remove unstable metal-based nanoparticles formed during thermal treatment (e.g., carbides, oxides, and pure-metallic phases), enhancing the exposure of catalytically active MN_x (x = 2–5) sites.[45,47,50,53–56]

Pyrolysis under NH_3 can further increase microporosity and introduce basic N-functionalities, which can boost the ORR activity but often at the expense of long-term stability.[53,57] Charreteur et al.[57] showed that the pyrolysis atmosphere significantly impacts Fe–N–C catalyst performance. Using iron tetramethoxyphenylporphyrin (FeTMPP) supported on carbon black N-330 and pyrolyzed at 950 °C, they showed that the NH_3-treated catalyst delivered higher initial ORR activity at pH = 1 (17.1 mA mg^{-1} at 0.8 V_{RHE}), but poor stability. In contrast, the Ar-treated catalyst showed lower activity (1.9 mA mg^{-1} at 0.8 V_{RHE}), but superior durability. The enhanced electrocatalytic activity after NH_3 treatment was linked to increased microporosity, while improved stability in Ar was attributed to greater graphitization. Similar trends were observed by Meng et al.,[58] reinforcing the trade-off between activity and stability. While NH_3 serves as an external nitrogen source, the macrocyclic ligands themselves also contribute to nitrogen doping, with varying effects on the electrocatalytic performance. Roncaroli et al.[59] systematically investigated how nitrogenated heterocyclic ligands (ranging from five to six-membered rings with one to four N atoms, including tetra-4-carboxyphenyl-porphyrin, TCPP) affect the ORR activity of pyrolyzed Fe- and Co-based catalysts supported on Vulcan carbon XC-72. The complexes were pyrolyzed at 500, 700, and 900 °C under N_2, yielding the highest activity in acidic media at the optimal temperature of 700 °C. Polypyridinic ligands like phenanthroline (phen) outperformed TCPP, enhancing the activity, kinetics, and selectivity of the final catalyst. Although Fe-phen and bimetallic FeCo-phen catalysts showed lower peroxide yield, they

underperformed compared to Co-phen in terms of onset potential and kinetics. The highest ORR activity was linked to a greater N-retention (notably pyridinic-N) and reduced CoO content. However, the stability of Fe- and FeCo-based catalysts was not assessed, despite their promising selectivity.

Among MN_4 macrocycles, the most studied correspond to Fe and Co phthalocyanines and porphyrins,[45,47,48,60–62] which have well-known molecular structures enabling one to carry out systematic studies on pyrolysis processes to obtain efficient ORR electrocatalysts. Although M–N–C catalysts can initially match the ORR activity of Pt/C, their long-term stability, especially in PEMFCs, remains a major limitation. Fe-based pyrolyzed catalysts exhibit high initial activity and selectivity toward the 4-electron pathway, but their stability suffers under acidic conditions (pH < 4). This is due to Fe-mediated Fenton reactions, which decompose H_2O_2 into reactive oxygen species that degrade the carbon support.[63] To improve durability, bi- and tri-metallic M–N–C systems incorporating Co and/or Mn have been developed. While these metals enhanced stability by suppressing Fenton-type reactions, they often exhibit lower selectivity for the direct 4-electron pathway compared to Fe–N–C catalysts, resulting in hydrogen peroxide yields under certain conditions.[63] Introducing both Fe and Co into a single pyrolyzed catalyst has shown synergistic effects, improved ORR activity, selectivity, and stability compared to monometallic counterparts.[64] Jiang and Chu[65] synthesized a CoFe–N–C catalyst by pyrolyzing a mixture of hemin and cobalt(II) tetramethoxyphenylporphyrin (CoTMPP) impregnated on Vulcan carbon XC-72R at 700 °C under N_2. In half-cell tests, the catalyst exhibited onset potentials of 0.75 V_{RHE} (acidic) and 0.85 V_{RHE} (alkaline), following a 2 + 2 electron pathway (initial O_2 reduction at Co sites to H_2O_2, followed by further reduction to H_2O at Fe sites). When integrated into a membrane electrode assembly (MEA), the catalyst showed a stability trend of acidic > neutral > alkaline, outperforming the Fe–N–C analogue. Similarly, Kumar et al.[66] reported the excellent ORR activity for pyrolyzed M–N–C catalysts (800 °C under N_2) derived from Fe-, Co-, Ni-, and Mn-phthalocyanine supported on multiwalled carbon nanotubes (MWCNTs). The FeCoN-MWCNT variant achieved the highest onset potential in alkaline media (0.93 V_{RHE}), linked to the formation of highly active MN_x sites. Sun et al.[55] developed a trimetallic Co$_3$Fe$_7$/N, Mn-PC catalyst by pyrolyzing a mixture of CoTMPP, hemin, manganese acetate, and dicyandiamide, followed by acid leaching. The resulting material, composed of Co$_3$Fe$_7$ alloy nanoparticles embedded in a Mn- and N-doped porous carbon matrix, exhibited superior ORR activity in alkaline media, with an onset potential of 0.98 V_{RHE}, outperforming mono- and bimetallic analogs. This improvement was attributed to intermetallic synergy, an optimal ratio of graphitic-N and pyridinic-N, and a high electrochemically active surface area, enabling a 4-electron pathway. The active sites were proposed to consist of Co$_3$Fe$_7$ nanoparticles and Fe/Co–N$_x$ moieties, while Mn- and N-doping enhanced electrical conductivity by tuning the electronic structure. The catalyst also showed excellent methanol tolerance and

stability, exceeding the performance of commercial Pt/C under alkaline conditions.

2.2. Structural evolution and site preservation during pyrolysis of MN₄ macrocycles for obtaining M–N–C catalysts

Although pyrolysis often introduces structural rearrangements and partial loss of molecular identity, several studies have shown that MN_4 macrocycle cores can be preserved or converted into well-dispersed MN_x (x = 2–5) sites embedded within nitrogen-doped graphitized carbon matrices.[45,47,48,67] These matrices typically contain graphitic-N, pyridinic-N, and pyrrolic-N species, which contribute to electronic conductivity and activity. The resulting MN_x sites are regarded as the primary ORR-active centers and are commonly classified as single-atom catalysts (SACs), operating predominantly through a 4-electron pathway.[2] Among the different nitrogen species, pyridinic-N is particularly effective in promoting peroxide reduction to water, acting as a secondary active site.[9] The MN_4-site preservation during pyrolysis depends on the temperature and precursor design. Some studies suggest that pyrolyzing metallomacrocycles below 600–700 °C favors retention of MN_4 motifs with high atomic dispersion, whereas annealing at higher temperatures (>700 °C) often causes their decomposition into less-defined species and favors the formation of metal nanoparticles due to agglomeration.[45,62,67–70] Such nanoparticle formation reduces the accessibility of the MN_x sites and may consequently impair ORR activity. Other studies have shown that MN_4 motifs can persist even after high-temperature pyrolysis, provided that the precursor design is carefully controlled.[71–73] However, the final structural outcome strongly depends on multiple factors, including the synthesis route, precursor concentration, pyrolysis conditions, and axial ligand modification. Anchoring an axial ligand to an in-plane square-planar MN_4 site results in a distorted square-pyramidal MN_5 geometry. This axial coordination modifies the ligand field and electronic density at the metal center, thereby influencing the adsorption energies of oxygenated intermediates and tuning the M(III)/M(II) redox potential, ultimately impacting ORR activity.[74,75]

More broadly, strategies aimed at incorporating axial ligands (e.g., O, S, N, or halogens) to expand the coordination sphere of MN_x sites have emerged as a promising approach to enhance the intrinsic ORR activity of the metal center. Such approaches include the rational design of precursors containing pre-coordinated axial ligands prior to pyrolysis, as well as post-synthetic adsorption or solution impregnation treatments applied to the pyrolyzed catalysts.[74,75] However, achieving precise synthetic and thermally stable five-coordination environments under high-temperature pyrolysis conditions remains a significant synthetic challenge.

In parallel to coordination expansion strategies, careful engineering has also proven effective in preserving well-defined MN_4 motifs during pyrolysis. For instance, Zhai et al.[51] demonstrated that ionic self-assembly of Fe(III) mesotetra(N-methyl-4-pyridyl)porphine (FeNMePyP) and Co(III) meso-tetra(4-sulfonatophenyl)porphine (CoTPPS4), impregnated onto carbon EC-600 (60% loading) and pyrolyzed at 650 °C under an inert atmosphere, produced a highly active ORR catalyst with preserved FeN₄ and CoN₄ sites (Fig. 1a). The catalysts exhibited an E_{onset} of 1.01 V_{RHE} in alkaline media (Fig. 1b), operating via a 4-electron pathway and showed excellent durability and methanol tolerance. The high
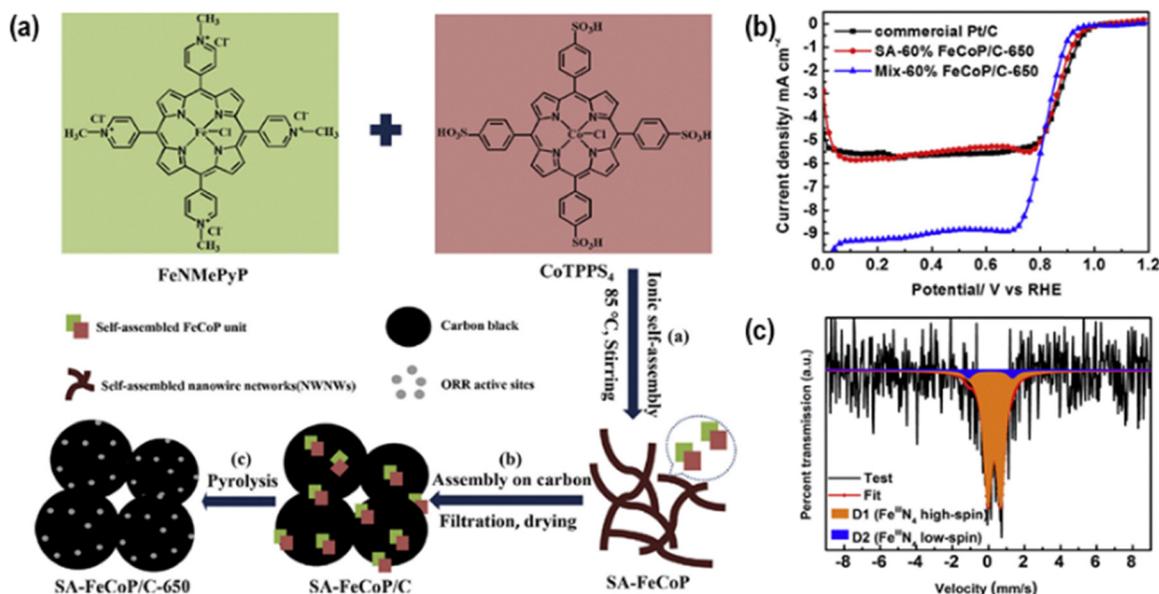
Fig. 1 (a) Schematic representation of the synthesis of ionic self-assembly and the pyrolysis process of Fe- and Co-macrocycles supported on carbon substrate. (b) ORR polarization curves in alkaline media of the pyrolyzed catalysts (SA = self-assembly synthesis methodology; Mix: mechanical mix synthesis methodology). (c) ^{57}Fe Mössbauer spectra of the pyrolyzed catalyst synthesized using the SA process. Reproduced from ref. 51 with permission from Elsevier, copyright 2021.

performance was attributed to ionic interactions between the oppositely charged macrocycles and π–π stacking with the carbon support, promoting uniform self-assembly and controlled thermal transformation. This prevents the formation of metal nanoparticles, as confirmed by XRD, and preserves the MN_4 cores, as evidenced by XPS. In contrast, mechanically mixed controls showed lower onset potentials due to metal agglomeration. [57]Fe Mössbauer spectroscopy further confirmed the exclusive formation of D1 and D2 Fe-sites (Fig. 1c), which are highly accessible and catalytically active. Similarly, Ye et al.[76] demonstrated that tailoring monomer connectivity (number of different sites to which the ligands connect) in macrocyclic precursors directly influences the coordination environment and electrocatalytic ORR performance in alkaline media, thereby validating the close correlation between catalyst structure and performance in these systems.

Recently, Muhyuddin et al.[62] investigated the structural evolution of Fe-based sites during pyrolysis using in situ X-ray absorption spectroscopy (XAS) combined with ex situ analyses of FePc supported on EC-600JD carbon (10% loading), pyrolyzed at 600 °C under an inert atmosphere. The X-ray absorption near edge structure (XANES) linear combination fitting confirmed the preservation of atomically dispersed FeN_x species within defective carbon matrices up to 600 °C (Fig. 2a). Beyond this temperature, FeN_4 moieties degrade, favoring nanoparticle formation and nitrogen loss, both factors being detrimental to ORR performance in acid and alkaline media. The highest ORR activity (E_{onset}, $E_{1/2}$, and J_L) correlated with elevated FeN_4 content, accompanied by minor fractions of FeN_3 and FeN_2 species and abundant pyridinic-N functionalities (Fig. 2b and c). Similar retention of FeN_4 sites at 600 °C has also been reported in bi-and tri-metallic pyrolyzed M–N–C

catalysts derived from Fe, Co, and Cu phthalocyanines.[70] These findings underscore the importance of carefully balancing thermal treatment conditions to maximize site preservation while minimizing coordination degradation.

Beyond structural preservation, heat treatment also induces electronic modifications. Several studies have shown that pyrolysis shifts the M(III)/(II) redox potential of the MN_4 catalysts toward more positive values, making the metal center "more noble" and harder to oxidize.[77] The M(III)/(II) redox potential has thus been proposed as a reactivity descriptor for ORR activity, as shown in several publications.[27,78] The fundamental understanding of molecular governing factors in nonprecious metal electrocatalysts for the ORR was reported by Ramaswamy et al.[79]

The mechanism of the ORR on the pyrolyzed nonprecious metal catalysts has been rationalized using an activity descriptor based on the principles of surface science, along with the coordination chemistry to establish a relationship with the redox potentials over the pyrolysis temperature (Fig. 3a). Upon heat-treatment of iron(III) meso-tetraphenylporphine chloride (FeTPPCl) at 800 °C, the $Fe^{2+/3+}$ redox potential significantly positively shifted, and the Fe–N–C catalyst tended to be more ORR active. Interestingly, the electrocatalytic ORR activity of the pyrolyzed Fe–N–C catalyst depended also on the carbon support material (Fig. 3c), which was explained by a change of the electron-withdrawing ability (Fig. 3b) and the degree of π-electron delocalization on disordered graphitic carbon. The intrinsic ORR activity, quantified in terms of turnover number at 0.8 V (Fig. 3d), further corroborates the structure–activity relationship. The proposed redox mechanism governing the ORR on pyrolyzed Fe–N_x/C is illustrated in Fig. 3e.
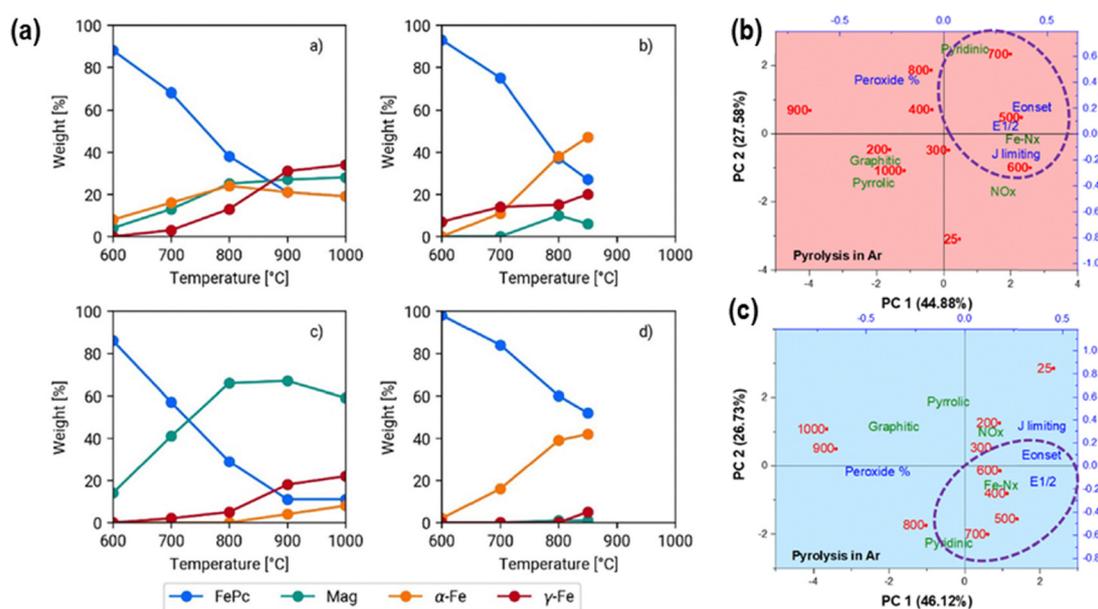
Fig. 2   (a) XANES linear combination fitting of the pyrolyzed (600 °C) FePc on EC-600JD carbon. Biplots acquired through principal component analysis (PCA) show the relationships among the surface-active moieties detected by XPS and the performance parameters of FePc-derived catalysts at different temperatures during pyrolysis under Ar in (b) acidic and (c) alkaline electrolytes. Reproduced from ref. 62 with permission from Elsevier, copyright 2024.
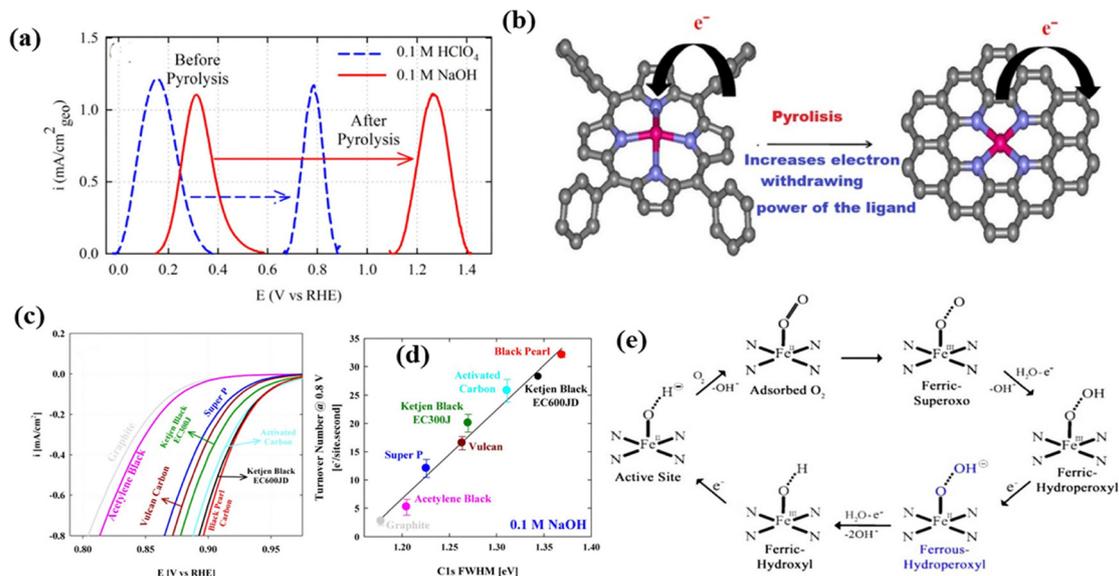
Fig. 3 (a) Square-wave voltammetry profiles of the Fe−N$_x$ catalyst supported on black pearl carbon before and after pyrolysis at 800 °C in 0.1 M HClO$_4$ and 0.1 M NaOH electrolytes. (b) Structural models of the active site structures before and after pyrolysis at 800 °C. Color codes in structural models: red, iron; blue, nitrogen; gray, carbon; white, oxygen. (c) ORR activity of the Fe−N$_x$/C catalyst (pyrolyzed at 800 °C) on various carbon supports in O$_2$-saturated 0.1 M NaOH electrolyte at a rotation rate of 900 rpm and a scan rate of 20 mV s^{-1}. (d) Linear relationship between ORR turnover numbers in 0.1 M NaOH electrolyte versus full-width at half-maximum of C 1s photoemission spectra. (e) Catalyst cycle showing the redox mechanism involved in the ORR on pyrolyzed Fe−N$_x$/C active sites in dilute alkaline medium. Reproduced from ref. 79 with permission from the American Chemical Society, copyright 2013.

Consequently, the ORR activity of MN$_4$ macrocycle-derived M−N−C catalysts is governed not only by site density but also by coordination geometry, local electronic structure, and support-induced electronic modulation. Collectively, these findings indicate that pyrolysis should be viewed as a coordination-engineering process capable of generating and stabilizing distinct MN$_x$ environments, including FeN$_5$ configurations, with different electrocatalytic behavior. Therefore, elucidating the interplay between M−N coordination, electronic structure, and electrochemical descriptors remains essential for the rational design of high-performance M−N−C catalysts.

2.3. The ORR multiple reactivity descriptors in MN$_4$ macrocycle-derived M−N−C catalysts

The simplest reactivity descriptor for MN$_4$ macrocycles is the number of d-electrons when comparing MN$_4$ complexes sharing the same ligand.[27,80] A volcano-shaped correlation has been observed for the ORR activity for both metallophthalocyanines and metalloporphyrins, but the optimum metal for phthalocyanines is Fe, while for porphyrins it is Co. It is possible that the position of the maximum could change depending on the applied potential and the M(III)/(II) redox potential of the catalysts that will control the fraction of M(II) active states at a given potential. However, for Co it seems to be the Co(II)/(I) redox potential that controls the activity.

A classical reactivity descriptor in electrocatalysis is the site-reactant intermediate binding energy, in this case using the M−O$_2$ binding energy, a plot of log(i)$_E$ versus this descriptor gives volcano-type plots, where the highest activity is observed for intermediate binding energies, following the well-known Sabatier Principle, which states that optimum activity is observed for binding energies not too strong and not too weak.[80] Too weak binding results in insufficient activation of the reactant's bonds. For too strong binding, the reaction products are too stable and cannot desorb from the active sites. The optimum condition corresponds to a binding energy of bound reactant that is equal to half the bond energy, which is to be formed or broken, i.e.: [M(II)]$_{ad}$ + O$_{2(aq)}$ ⇆ [M(III)]−O$_2^-$$_{ad}$ ΔG_{ad} = 0 (ligand is omitted for simplicity).

However, the binding energies are generally calculated in the absence of an electrolyte and electrode potential, and the latter can affect the surface concentration of M(II) active sites. A more practical reactivity descriptor is the M(III)/(II) redox potential, which can be measured under the same experimental conditions at which the activities are determined,[80] i.e., an overpotential and the presence of the electrolyte. When log(i)$_E$ is plotted versus the M(III)/(II) redox potential, a volcano plot is observed. However, more recently it has been reported that, especially for Co intact complexes (not heat-treated), a better fit is observed if the Co(II)/(I) redox potential is considered.[81] The strong binding region or descending region in the volcano correlation is explained according to the Sabatier Principle but does not seem to be realistic as discussed by Zagal and co-workers,[80,82] and the latter reports turnover frequency (TOF) values calculated on the basis of surface concentration of M(II) active species at the electrode potential used for comparison show an increase of this parameter in the descending region of the volcano and the volcano plot becomes a linear plot.

Recently, a new reactivity descriptor for the ORR has been proposed, the "electrochemical hardness" (ΔE^h).[83–85] This concept has been used to explain the reactivity of a series of FeN_4 macrocyclic complexes in a wide range of pH values. The electrochemical hardness is defined as the potential separation between the redox processes $E^\circ_{M(III)/(I)}$ and $E^\circ_{M(II)/(I)}$ of surface-confined MN_4 macrocycles, measured in the absence of O_2 and in aqueous media. These studies have been performed in both acidic and alkaline solutions. For the specific case of FePc, the second one-electron redox process has been attributed to an electron-transfer occurring on the ligand, i.e., $E^{\circ'}_{Fe(II)Pc/Fe(II)Pc-1}$.[84] Experimental results indicate that the ORR activity, expressed as $(\log j)_E$, diminishes when the "electrochemical hardness" increases.[84,85] Intact MN_4 macrocyclic complexes, as discussed above, have served as useful model catalysts to identify several reactivity descriptors. However, for practical application, they lack the long-term stability required for polymer electrolyte fuel cell performance, especially in acidic media.

Yang et al.[86] reported that pyrolysis of axial imidazole-coordinated iron 5,10,15,20-tetra(2-thienyl)porphyrin (FeTThP) supported on carbon black at 800 °C under an inert atmosphere yielded dispersed FeN_5 sites. The resulting catalyst showed enhanced ORR activity in alkaline media ($E_{1/2}$ = 0.89 V_{RHE}) compared to its sulfur-free analogue (Fig. 4a). The extended X-ray absorption fine structure (EXAFS) analysis confirmed the formation of axially coordinated FeN_5 sites (Fig. 4b), suggesting that the combined effect of axial coordination and S-doping within the graphitized carbon matrix synergistically modulates the electronic structure of the active Fe centers. This study highlights the importance of precursor architecture in inducing coordination expansion within Fe–N–C catalysts.[74] Pyrolysis at 800 °C in an inert atmosphere of iron(III) 2,3,7,8,12,13,17,18-octaethylporphyrin chloride (8EtFeP) and iron(III) 5,10,15,20-tetraphenylporphyrin chloride (4PhFeP) supported on Vulcan Carbon XC-72 significantly enhances the ORR activity compared to unpyrolyzed precursors (Fig. 4c).[87] The ORR onset potentials of these materials align closely with the Fe(III)/Fe(II) redox couple as discussed above.[77,80] This improvement is attributed to the stabilization of FeN_4 units within N-doped graphitized carbon matrices, which exert electron-withdrawing effects on the metal centers (Fig. 3b and 4d). The electron-withdrawing effect shifts the Fe(III)/(II) redox potential to more positive values, which increases the electrocatalytic activity for the ORR.[77,79,88] Pyrolysis shifts the onset potentials by ~100 mV to more positive values relative to the pristine complexes (Fig. 4e and f).[87] A similar trend is observed for Co-based analogs, where pyrolysis raises the $E^\circ_{Co(III)/Co(II)}$ and, accordingly, the ORR onset potential in both acidic and alkaline media (Fig. 4g).[89] In the Fe-based systems, the ORR follows either a direct 4-electron or 2 × 2 pathway, while Co-based catalysts tend to show mixed selectivity, producing both H_2O_2 and H_2O. In all cases, the ORR activity increases as the redox potential of the MN_4 (or MN_x) sites becomes more positive, following a linear $\log(j) - E^\circ_{redox}$ correlation (Fig. 4h),
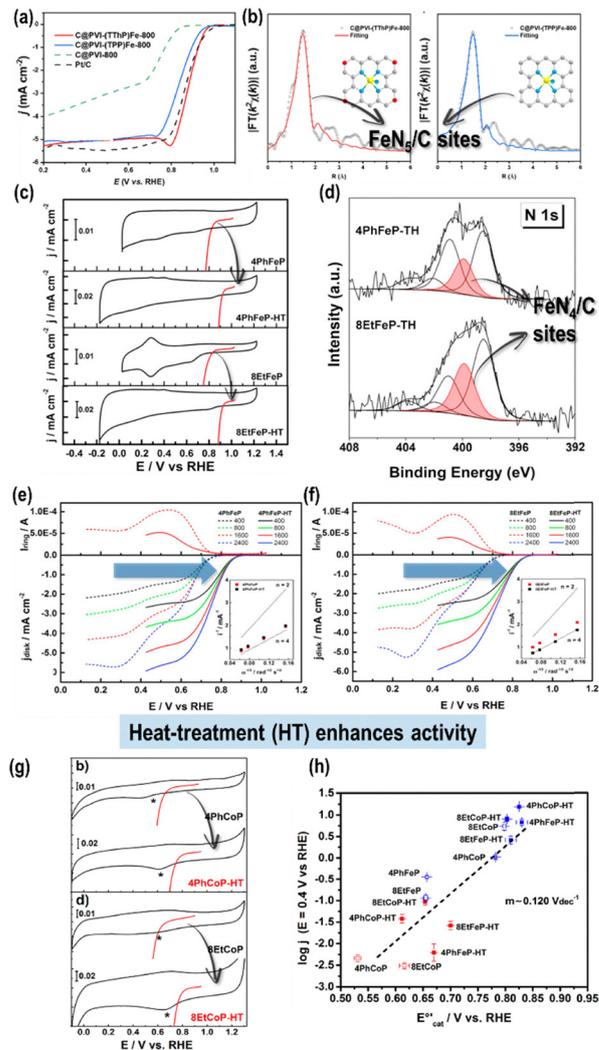
Fig. 4 (a) ORR polarization curves for the Fe–N–C catalysts in O_2-saturated 0.1 M KOH solution at 1600 rpm. (b) FT-EXAFS R-space fitting curves of the obtained Fe–N–C catalysts, including a structural model of Fe–N_5. Reproduced from ref. 86 with the permission from the American Chemical Society, copyright 2024. (c) Cyclic voltammograms for unpyrolyzed and pyrolyzed porphyrinic-based 4PhFeP and 8EtFeP catalysts in N_2-saturated alkaline media (black line), including kinetic currents (1600 rpm, 0.005 V s^{-1}) for the ORR (red lines) in O_2-saturated alkaline media. (d) N 1s XPS spectra of 4PhFeP and 8EtFeP pyrolyzed at 800 °C. Electrocatalytic activity comparison toward the ORR for unpyrolyzed and pyrolyzed (e) 4PhFeP and (f) 8EtFeP catalysts in O_2-saturated 0.1 M NaOH. Reproduced from ref. 87 with the permission from Elsevier, copyright 2019. (g) Cyclic voltammograms for unpyrolyzed and pyrolyzed phthalocyanine-based 4PhCoP and 8EtCoP catalysts in N_2-saturated acidic media (black line), including kinetic currents for the ORR (red lines) in O_2-saturated 0.1 M H_2SO_4 (1600 rpm, 0.005 V s^{-1}). (h) Linear correlation between $\log(j)$ at 0.4 V (vs. RHE) and E°_{redox} of the unpyrolyzed Fe- and Co-based porphyrinic catalyst (open symbols) and pyrolyzed catalyst (closed symbols). Red and blue symbols indicate the values measured under acidic and alkaline media, respectively. Reproduced from ref. 89 with the permission from Elsevier, copyright 2020.

consistent with non-pyrolyzed macrocycle trends.[80] These results confirm that $M(II)N_4$ or $M(II)N_x$ sites remain the dominant active centers in both acidic and alkaline media, with the

graphitized N-doping lowering the M-O$_2$ binding energy and enhancing catalytic efficiency.[80,90]

Domínguez et al.[91] impregnated Fe, Co, and Mn phthalocyanines onto N-doped activated carbon and pyrolyzed the mixture at 800 °C under N$_2$. After acid-washing, the ORR activity in acidic media followed the trend Fe > Co > Mn. This was attributed to higher N-content and increased surface area, which improved the accessibility and dispersion of MN$_x$ active sites. Notably, the trend also correlates with the number of d-electrons, a well-established reactivity descriptor for MN$_4$ macrocyclic complexes such as phthalocyanines and porphyrins.[80,90]

2.4. Sustainable approaches for obtaining MN$_4$ macrocycle-derived M–N–C catalysts

In an effort to lower the production costs and align with circular economy principles, Giulini et al.[92] explored the use of waste polypyrromethenes, by-products from the Adler–Longo synthesis of porphyrins (80% yield), as a precursor for Fe-based pyrolyzed ORR catalysts. Both purified porphyrins and the corresponding waste were impregnated onto EC-600 carbon and pyrolyzed at 600 °C under an inert atmosphere. The resulting Fe–N–C catalysts showed comparable ORR activity, with onset potentials of 0.937 and 0.972 V$_{RHE}$ in alkaline electrolyte, proceeding via 2 × 2 and 4-electron pathway with minimal hydrogen peroxide formation. This study demonstrated the viability of macrocycle synthesis by-products for fabricating efficient ORR electrocatalysts. Similarly, biomass-derived carbon supports have gained attention for enhancing surface area and improving FeN$_x$ site accessibility.[93–95] For instance, FeTPP was combined with pre-carbonized, Si-rich rice husk and pyrolyzed at 800 °C in an inert atmosphere to yield Fe–N–C catalysts co-doped with Si, S, and P. Among them, the FeN/SSiRC catalyst exhibited the highest performance, with a half-wave potential of 0.885, 0.773, and 0.682 V$_{RHE}$ in alkaline, acidic, and neutral media, respectively. This was attributed to a high density of exposed FeN$_x$ sites and synergistic effects from pyridinic-N, Si, and S dopants, which were shown via DFT calculations to lower the ORR energy barrier.

2.5. Porous and structured supports used for the thermal treatment of MN$_4$ macrocycle-derived M–N–C catalysts

In some cases, hard templates such as silica or magnesium oxide have been employed to produce highly active catalysts with enhanced mesoporosity, which improves mass transport and accessibility to active sites.[93,96,97] More recently, metal–organic frameworks (MOFs) have been explored as precursors to further increase surface area, improve site dispersion, and boost the density of atomically dispersed MN$_x$ active sites. For instance, MOF-5 and ZIF-8 have been employed as supports for metallomacrocycles such as FeTPP[98] and FePc,[99] to produce efficient ORR catalysts in alkaline media. Their high electro-catalytic activity is attributed to the large surface area, which enhances FeN$_x$ site accessibility, and the synergistic effect of secondary N-doping and residual metal nanoparticles.

Additionally, porphyrinic-MOFs have gained interest as precursors for obtaining pyrolyzed M–N–C catalysts. Jiao et al.[100] synthesized a Fe–N–C catalyst by pyrolyzing MOF-545 at 800 °C in an inert atmosphere (Fig. 5a), yielding a high density of isolated FeN$_4$ sites. The absence of Fe nanoparticles and the presence of oriented mesoporous channels boosted active site exposure, leading to E_{onset} and $E_{1/2}$ values of 1.00 V$_{RHE}$ and 0.89 V$_{RHE}$, respectively, in alkaline media, and 0.93 V$_{RHE}$ and 0.78 V$_{RHE}$, in acidic media (Fig. 5b and c). In a related study, a Zn-CoTCPP catalyst was prepared from [Zn$_2$(COO)$_4$] paddle-wheel SBUs and cobalt-tetrakis(4-carboxyphenyl)porphyrin (CoTCPP), followed by pyrolysis at 400 °C in an inert atmosphere. The resulting material exhibited high CoN$_4$ site density (Fig. 5d), uniformly dispersed in a covalent-bonded quasi-carbon matrix, with the $E_{1/2}$ value of 0.82 V$_{RHE}$ in alkaline media (Fig. 5e), making it a promising candidate for ORR applications.[101]

3. MN$_4$ macrocycle-derived cathodes for AEMFC and PEMFC applications

For a decade, numerous research studies have been conducted using different MN$_4$ macrocycle-derived catalyst materials for the improvement of polymer electrolyte fuel cell performance in search of alternative cathodes for Pt-based catalysts although the pioneering work by Jasinski on cobalt phthalocyanine-based ORR electrocatalyst dates back to 1964.[42] On account of the structural benefits of MN$_4$ moieties, the efficient ORR activity and stability, attraction has been focused in recent times on addressing the durability hurdles, specifically under acidic conditions.[102–104] The ORR activity data determined from RDE experiments and the AEMFC[32,105,106] and PEMFC[107] performances of the cathode catalysts are summarized in Tables 1 and 2, respectively. The following subsections (3.1 and 3.2) specifically discuss recent advances in MN$_4$ macrocycle-derived catalysts investigated as cathodes for AEMFCs and PEMFCs, with emphasis on their structural design, performance optimization, and durability under relevant operating conditions.

3.1. Template-assisted and confinement strategies for MN4 macrocycle-derived M–N–C cathodes

Sa et al.[111] reported the fabrication of Fe–N–C single-atom catalysts by proposing a silica-protective-layer-mediated pyrolysis method for preferential formation of catalytically active Fe–N$_4$ moieties in Fe–N–C material by effectively preventing the formation and agglomeration of inorganic Fe-based nanoparticles during the pyrolysis process (Fig. 6a and b). The resulting CNT/PC catalyst showed good ORR activity in both alkaline and acidic media (Fig. 6c), and demonstrated better fuel cell performances in both AEMFCs and PEMFCs (Fig. 6d and e). Moreover, structural uniformity of Fe–N$_x$ sites made them a model system for precise control of their coordination environments and configurations, exposing more active sites, and promoting the efficient mass transport for a deeper understanding of the electrocatalytic properties of the catalysts.
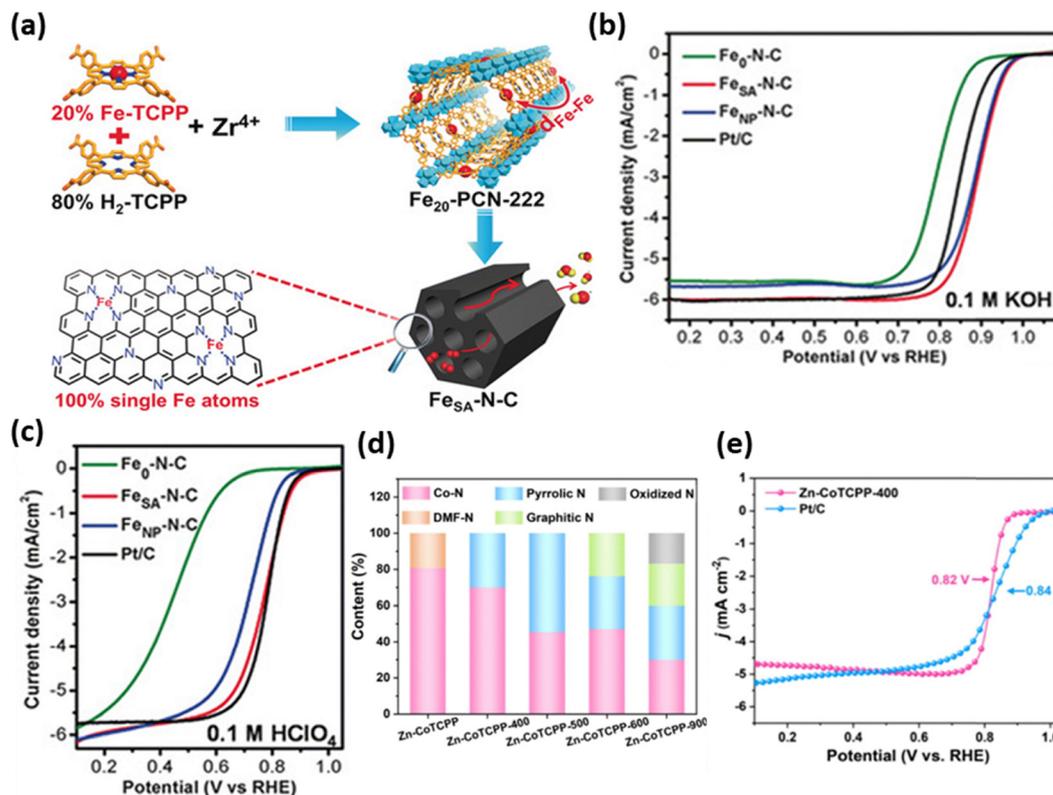
Fig. 5 (a) Schematic representation of the synthetic route for obtaining the Fe−N−C catalyst using MOF-545, including FeTCPP and H_2TCPP moieties. Linear sweep voltammetries obtained for the MOF-545-derived catalysts in (b) alkaline and (c) acidic media. Reproduced from ref. 100 with the permission from John Wiley and Sons, copyright 2018. (d) Normalized content of deconvoluted N-species quantified by high-resolution N 1s XPS. (e) LSV curves for the Zn-CoTCPP-400 electrocatalyst in O_2-saturated 0.1 M KOH. Reproduced from ref. 101 with the permission from Elsevier, copyright 2025.

Similarly, Woo *et al.*[114] synthesized Fe,N-doped carbon catalysts *via* a silica coating-mediated pyrolysis-based strategy using 2,1,3-benzothiadiazole and triphenylphosphine as S and P precursors, respectively, with iron acetate/1,10-phenanthroline, and carbon nanotubes (CNTs). Both S and P-containing catalysts showed high ORR electrocatalytic activity, but interestingly the S-containing catalyst outperformed the P-doped catalyst in a single-cell AEMFC test. The XANES and EXAFS analyses suggested that the silica-coating strategy proved to be useful for inhibiting the Fe aggregation and improved the density of Fe–N_x sites, resulting in improved ORR activity compared with the uncoated one. The Fe–S-Phen-CNT catalyst achieves an impressive maximum power density (P_{max}) of 635 mW cm^{-2}. By integrating a nitrogen-rich precursor such as spent coffee grounds (SCGs) with the synergistic interaction of atomically dispersed Fe and Mn, bimetallic SCG-derived electrocatalysts were developed with enhanced ORR activity.[127] The graphene aerogel-supported materials act as efficient electrocatalysts by effectively suppressing the restacking and agglomeration of graphene sheets. This study not only shows the promise of a pyrolysis-free synthesis strategy for developing cost-effective catalysts, but also highlights the critical role of catalyst layer architecture in fully realizing the performance potential of non-precious metal catalysts for AEMFC applications.[128]

The strategy of tailoring the catalyst layer architecture through polymer composite platforms offers a new and versatile pathway for implementing a wide range of molecular catalysts in fuel cell applications.[125] Using a complete suite of analytical techniques can establish the pivotal role of tailored material design, structural characteristics, and synthesis strategies in defining electrocatalytic performance toward the ORR in AEMFCs. In particular, the controlled integration of silica and metal species, the removal of structure-directing agents, and the use of nitrogen-rich precursors are shown to regulate the catalyst morphology, pore architecture, and chemical composition.[126,129] Recently, Dekel and co-workers,[109] reported the pyrolysis-free preparation of Ketjen Black (KB) supported MPc-based catalysts (M = Fe, Mn, Co, Cu, Ni, Li, Sn) through a single-step, room-temperature ultrasonication process that provides valuable insight for efficient catalyst design and the broader adoption of transition metal phthalocyanine-based catalysts and AEMFC technology.

Praats *et al.*[116] synthesized a cobalt-containing catalyst using Co phthalocyanine (CoPc) as a precursor on a carbon nanotube and carbide-derived carbon (CDC) support prepared from two sources (*i.e.*, titanium carbide and silicon carbide), where the Si-CDC-supported catalyst was found to exhibit enhanced ORR activity. Detailed analysis suggests a greater amount of nitrogen species on the Si-CDC-supported catalyst as compared to the

Table 1 Summary of the ORR parameters from half-cell tests in alkaline media and H_2–O_2 AEMFC performance for the MN_4 macrocycle-derived non-precious metal cathode catalysts

Catalyst	Half-cell RDE data		H_2/O_2 AEMFC data		
	E_{onset} (V) vs. RHE	$E_{1/2}$ (V) vs. RHE	OCV (V)	P_{max} (mW cm^{-2})	Ref.
D-MN$_4$-CNF-IL-A	0.97	0.86	1.05	231	108
FePc/KB	0.96	—	0.98	524	109
MnPc/KB	0.86	—	0.93	248	109
CoPc/KB	0.84	—	0.95	605	109
NiPc/KB	0.82	—	0.81	350	109
FeNiN-MWCNT	0.94	0.87	1.0	406	110
CNT/PC (Fe)	0.97	0.88	0.96	380	111
FePc/C (600 °C)	0.95	0.88	0.88	123	112
CoFeN$_x$/C	0.95	0.84	0.87	38	65
MnPc/C	0.72	0.55	0.90	97	113
FePc/C	0.87	0.70	0.83	87	113
CoPc/C	0.79	0.70	0.87	105	113
NiPc/C	0.69	0.59	0.90	88	113
Fe−Phen/CNT	0.99	0.90	1.00	410	114
Fe−P−Phen/CNT	0.99	0.91	1.00	570	114
Fe−S−Phen/CNT	0.99	0.91	1.00	635	114
FeCoN-MWCNT	0.93	0.86	0.98	692	66
FeMnN-MWCNT	0.93	0.85	0.95	582	66
Fe@Fe−N−C	0.99	0.82	—	242	115
SiCDC/CNT(1:3)/CoPc	0.91	0.81	0.94	473	116
SHUb-Fe/N-A	0.94	0.80	1.01	234	54
SHUb-Co/N-A	0.93	0.80	0.98	232	54
SiCDC/CNT(1:3)/FePc	0.87	0.74	1.00	164	117
TiCDC/CNT(1:3)/FePc	0.93	0.77	1.00	182	117
pyrolyzed KB/FePc	0.94	0.76	1.00	186	117
FePc/MWCNT	0.86	—	0.98	60	118
CoPc/MWCNT	0.91	—	0.99	100	118
HT800-FeP aerogel	0.96	0.86	0.93	580	119

Ti-CDC counterpart. The CoPc-derived cathode catalyst revealed excellent AEMFC performance. In another study, Praats et al.[117] used FePc as a precursor for the preparation of Fe–N–C catalyst. The catalyst material consisting of TiC-derived carbon showed higher ORR activity than the catalyst based on the SiC-derived support. This leaves scope to probe the electronic properties of such materials to unlock their potential for better electrocatalytic ORR behavior. However, it is envisioned that this can be achieved by connecting material characterization and theoretical calculations in such a way that it can substantially impact and predict the performance of M–N–C catalyst materials.

3.2. Influence of pyrolysis on the structure and activity of MN_4 macrocycle-derived M–N–C cathodes

Our early work on heat-treated MWCNT-supported MPc-based catalysts showed decent ORR electrocatalytic activity in 0.1 M KOH and promising AEMFC performance (P_{max} of 100 and 60 mW cm^{-2} for CoPc/MWCNT and FePc/MWCNT cathodes, respectively).[118] The MPc-MWCNT mixture was pyrolyzed under an inert atmosphere at 800 °C to prepare ORR active and stable catalysts. Chung et al.[106] reported a low-temperature and gram-scale approach to synthesize FePc-embedded two-dimensional carbon sheets by annealing at 450 °C for an efficient cathode in AEMFCs. Generally, the employment of Fe–N–C electrocatalysts has been found to deliver excellent electrocatalytic ORR performance due to a suitable electronic structure and interaction with O_2 when the iron is coordinated to nitrogen in FeN$_x$ active sites.[106,130] Furthermore, it is well established that the electrocatalytic activity of the FePc is strongly associated with the specific interactions of the cations/anions at the electrolyte/ electrode interface, which influence the energy barriers and reorganization energies of the intermediates formed during the reaction.[84] Consequently, it becomes excellent models for studying and assessing the electronic factors on the Fe–N$_x$ site that affect the ORR performance, serving as an excellent functional molecular block to study reactivity descriptors for Fe–N– C catalysts. Zhu et al.[131] fabricated metal phthalocyanine (MPc) on a carbon support and tested it for AEMFC application. The MPcs (M = Co, Cu, Zn, and Ni) on Vulcan carbon were pyrolyzed at 600 and 800 °C and compared with non-pyrolyzed MPcs. The untreated MPcs revealed the following order of ORR activities: CoPc/C > CuPc/C > NiPc/C > ZnPc/C. For the 600 °C pyrolyzed catalysts, CoPc/C was found to be the most active one among the other catalysts studied. For the 800 °C treated materials, the activity order changed, and CuPc/C showed the highest ORR activity. The study reflects the large influence of heat-treatment temperature on the MPc/C catalyst activity. The MPc/C catalysts showed much lower fuel cell performances than that of Pt/C due to the complexity of the MEA preparation and the other influencing factors (such as the catalyst ink, spraying technology, hot-press temperature as well as the amount of binder).

Interestingly, several authors have tuned the redox properties of FePc using chemical substituents in their molecular

Table 2 Summary of the ORR activity from the half-cell tests in acidic media and PEMFC performance for the MN4 macrocycle-derived non-precious metal cathode catalysts

| Catalyst	$E_{1/2}$ (V) vs. RHE	Cell temp. (°C)	Back pressure (MPa)	Anode gas–cathode gas	Catalyst loading (mg cm^{-2})	P_{max} (mW cm^{-2})	Ref.
1000-III-NH$_3$-g	—	80	0.2	H_2–O_2	4	380	120
Co/N/C	—	50	0.2	H_2–O_2	10–12	150	121
NC Por_0.8–1050	—	80	0.2	H_2–O_2	4	600	122
Fe–N$_x$/C-NC1100	0.811	80	0.1	H_2–O_2	4	656	123
Fe–N$_x$/C-NC1100	0.811	80	0.1	H_2–air	4	312	123
COP$_{BTC}$-F	0.74	80	0.16	H_2–O_2	2	201	124
COP$_{BTC}$-F	0.74	80	0.16	H_2–air	2	147.4	124
L_FeMn	0.77	80	—	H_2–air	4.4	72	125
Fe-14MR/FePI	—	80	0.2	H_2–air	4,5	486	126
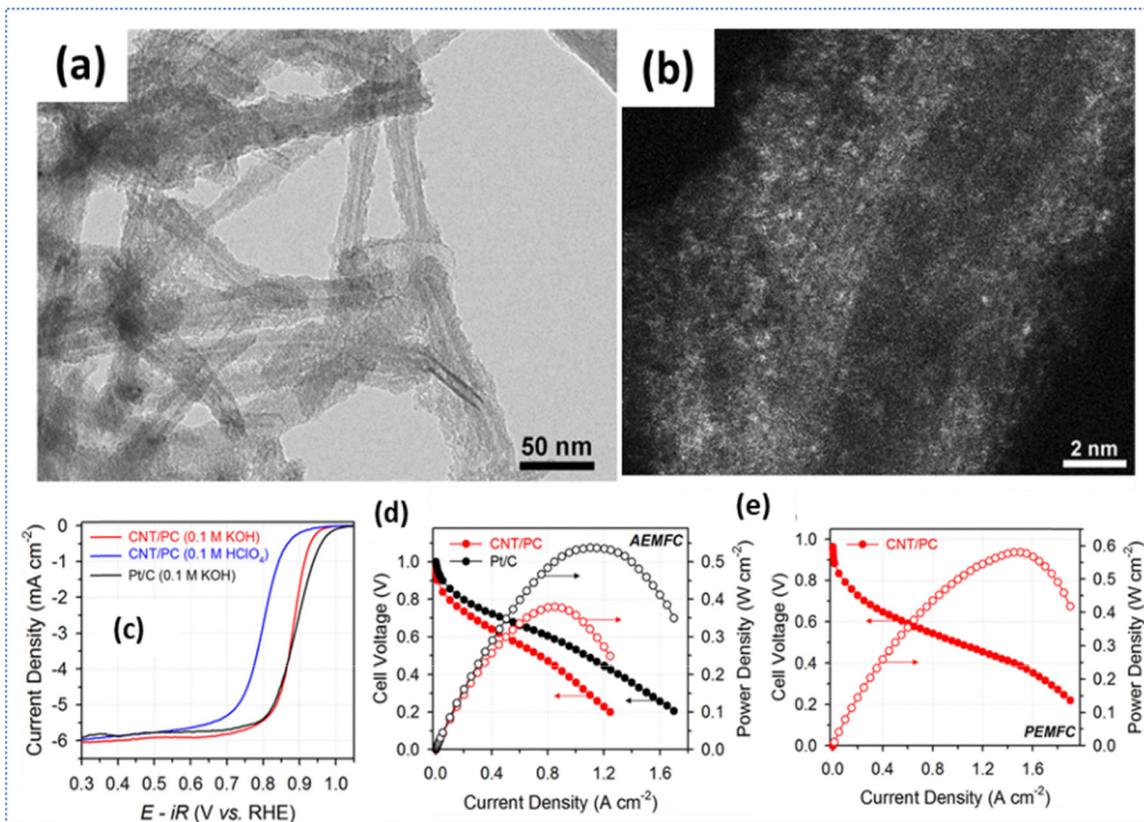
Fig. 6 (a) TEM and (b) HAADF–STEM images of CNT/PC. (c) ORR activity of CNT/PC. (d) AEMFC performances using the CNT/PC and Pt/C catalysts, and (e) PEMFC performance with the CNT/PC cathode catalyst. Reproduced from ref. 111 with the permission from the American Chemical Society, copyright 2016.

structure, for example electronegative fluorine atoms.[132] It was observed that the powerful electron-withdrawing nature of F-atoms promotes Fe–O_2 interaction during the ORR process as a result of a shift of the Fe(III)/(II) redox potential to more positive values compared to the unsubstituted FePc. Elbaz and co-workers[133] found enhanced electrocatalytic ORR activity in the electrochemical half-cell test, which was also translated into AEMFC performance as shown in Fig. 7a–d. The enhanced ORR activity and fuel cell performance were attributed to the synergistic interactions in the macrocyclic complex and efficient active centers created by the uniformly distributed atomic iron moieties. However, the study lacks a detailed elucidation of the physicochemical nature of the complex governing the ORR selectivity, activity, and durability in the F-substituted FePc-based catalyst. However, increasing the site density of M–N_4 centers always remains challenging; this limitation arises from the random distribution of M–N_4 sites during high-temperature pyrolysis, making precise control over their site density complicated. Yang et al.[134] introduced a high content of F-doping into the carbon substrate (6.29 at%), and assembled poly(iron phthalocyanine) on the prepared substrate to afford a highly efficient electrocatalyst for the ORR. The induced orbital coupling between electron-withdrawing fluorine atoms in the F-doped carbon substrates and the metal centers, promoted the delocalization of Fe d-orbital electrons.
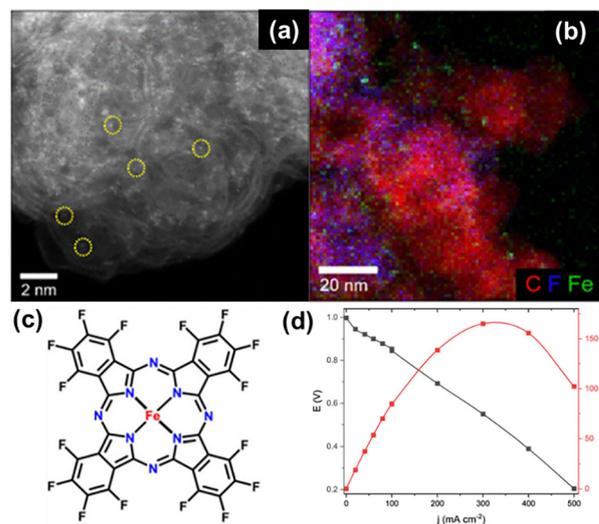
Fig. 7 (a) HAADF image and (b) corresponding EDS mapping. (c) Proposed structure of iron phthalocyanine substituted with fluorine. (d) Polarization curve (black) and power density curve (red) of FeFPc@BP2000 in AEMFCs. Operating conditions: 80 °C, 0.5 L min^{-1}, H_2/O_2, 2 mg cm^{-2} catalyst loading at the cathode, and 0.6 mg$_{Pt}$ cm^{-2} at the anode. Reproduced from ref. 133 with the permission from the American Chemical Society, copyright 2021.

The optimized PFePc/FC catalyst demonstrated enhanced ORR kinetics.

Kumar *et al.* prepared Fe and Ni phthalocyanine-derived bimetal electrocatalysts of various nanocarbon supports.[110] The mixture of MPcs and carbon nanomaterials was heat-treated at 800 °C under a N_2 atmosphere to obtain highly active electrocatalysts for the ORR. FeNiN-MWCNT and FeNiN-MC were reported to be the most active catalysts in 0.1 M KOH among the nanocarbon-supported MPc-based materials studied. Under AEMFC conditions, the FeNiN-MWCNT cathode exhibited the highest P_{max} of 406 mW cm^{-2}, followed by FeNiN-MC (P_{max} = 386 mW cm^{-2}). Also, the current density at the cell voltage of 0.6 V was higher for FeNiN-MWCNT (638 mA cm^{-2}) as compared to the FeNiN-MC catalyst (528 mA cm^{-2}). Muuli *et al.*[108] employed polyacrylonitrile-based electrospun carbon nanofibers (CNFs) as a support material for FePc and CoPc to achieve high electrocatalytic activity and good electrical conductivity for AEMFC performance. The influence of catalyst preparation conditions (*i.e.*, MPc content, presence of porogen, pyrolysis temperature, acid leaching) was investigated. The best electrocatalyst revealed a high $E_{1/2}$ value (0.857 V$_{RHE}$), good

durability ($\Delta E_{1/2}$ = 6 mV) in 0.1 M KOH and substantial P_{max} value of 231 mW cm^{-2} under AEMFC conditions. Muhyuddin *et al.*[125] used lignin-based biomass to produce activated porous char, which was functionalized with FePc and MnPc *via* a simplistic pyrolysis process to obtain monometallic and bimetallic electrocatalysts. The developed electrocatalysts performed well in both alkaline and acidic media, demonstrating their utility in both PEMFC and AEMFC systems.

However, the commonly used pyrolysis procedure typically destroys MN_4 centers present in metal phthalocyanines and porphyrins, but results in improved stability if the pyrolysis procedure is designed to prevent the loss of nitrogen species.[135] Miller *et al.*[112] studied the ORR activity of a FePc-based catalyst prepared at different pyrolysis temperatures. They observed that the ORR activity of the FePc/C catalyst decreased as the pyrolysis temperature increased above 600 °C. To obtain further insights, they utilized EXAFS analysis and reported that FeN_4 as the active sites for the ORR remained thermally stable up to 700 °C, but above 800 °C, the coordination number decreased, subsequently forming metallic iron nanoparticles causing decomposition of FeN_x species at higher temperatures and is
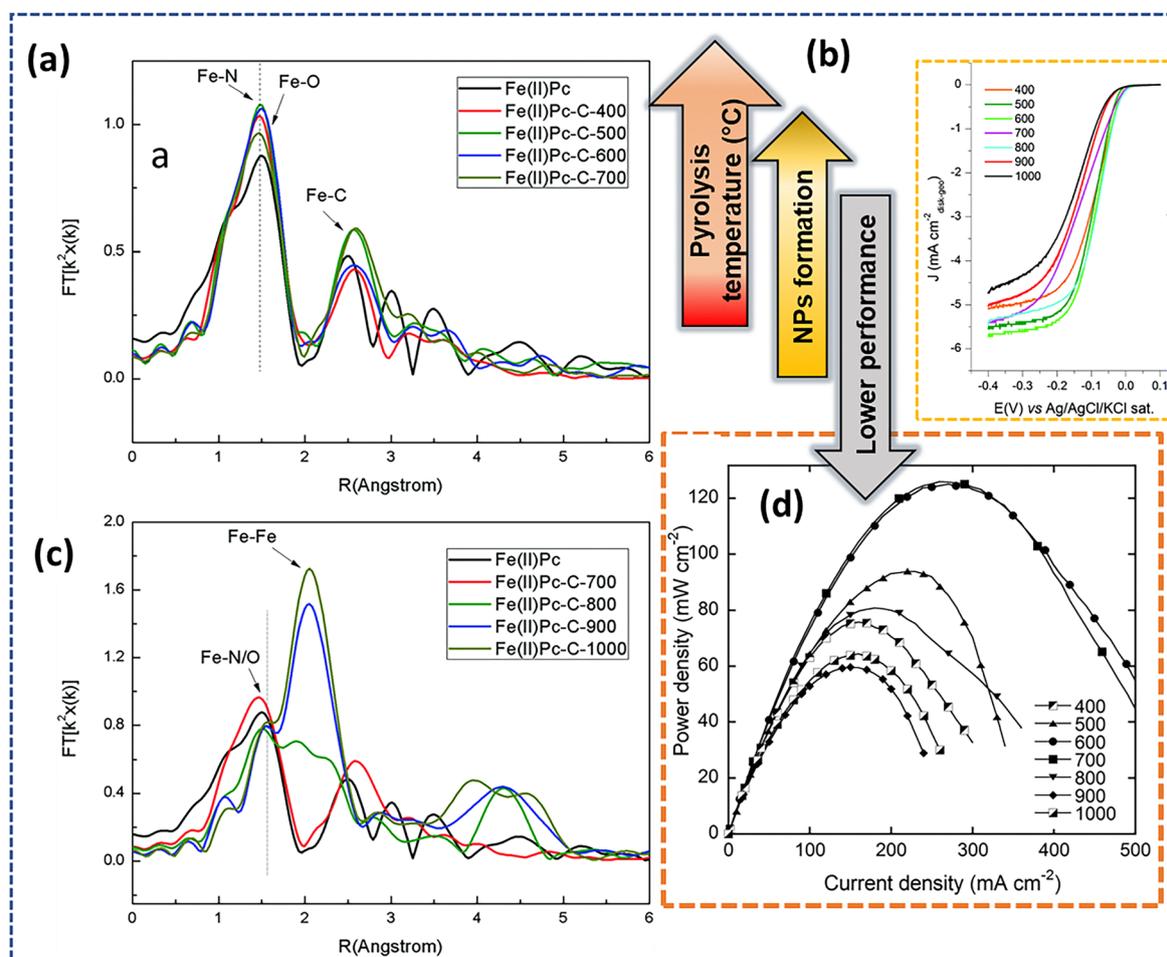
Fig. 8 Fourier transform of EXAFS of unpyrolyzed FePc and FePc samples pyrolyzed (a) up to 700 °C, and (c) samples pyrolyzed from 700 to 1000 °C. (b) ORR polarization curve in an O$_2$-saturated 0.1 M KOH solution, and (d) power density curves for H$_2$−O$_2$ AMFCs. *T* = 55 °C. H$_2$−O$_2$ (100% relative humidity, RH) with flow rates of 100 and 200 mL min^{-1}, respectively. Reproduced from ref. 112 with the permission from RSC Publishing, copyright 2016.

responsible for a decrease in the electrocatalytic ORR activity (Fig. 8a–d).

Chougule et al.[136] carried out a systematic optimization of pyrolysis conditions to establish the critical relationship between catalyst structure, active site configuration, and electrocatalytic performance. The optimized Fe–N–C/C catalyst exhibited high ORR activity and durability over prolonged electrochemical testing and displayed competitive single-cell AEMFC performance. Kumar et al.[66] presented a one-step pyrolysis method for the synthesis of mixed M–N–C-type catalysts, where iron phthalocyanine was used in combination with different metal phthalocyanines (e.g., FeNi, FeMn, and FeCo) and was studied for the ORR under alkaline conditions. The results suggest that FeCoN-MWCNT is the most active catalyst for the ORR. Also, the FeCoN-MWCNT catalyst exhibited a high peak power density value (692 mW cm^{-2}) in an AEMFC as compared to the other prepared catalysts (Fig. 9a–c). Persky et al.[137] reported another innovative bioinspired catalyst using a directed synthetic pathway to create adjacent Cu and Fe sites composed of a covalent 3D framework in an aerogel form. The aerogel-based catalyst exhibits high performance in a half-cell in 0.1 M KOH, with an onset potential of 0.94 V vs. RHE and a half-wave potential of 0.80 V vs. RHE, high selectivity toward

four-electron ORRs, and an iR-corrected peak power density of 0.51 W cm^{-2} was delivered in an AEMFC with an open circuit potential of 0.97 V (Fig. 9d). This study allowed the development of even more active, durable, and suitable electrocatalytic systems for high-performing fuel cells.

Nevertheless, if the afore-mentioned active moieties are buried within carbon layers, they will not actively participate in the ORR process.[138] Nabae et al.[126] utilized an organosynthetic approach to establish Fe–N–C catalysts as a support material for the Fe-14MR complex. This approach was designed to increase Fe–N$_4$ centers both on the outer surface and within the meso and micropores. As a result, their most optimized catalyst led to superior ORR kinetics in half-cell testing and showed promising results in PEMFC testing in terms of power density and stability for longer runs (Fig. 10a and b). Carbon aerogels are promising candidates for carbonaceous substrates for the large-scale preparation of M–N–C catalysts, due to their porous nature and high electrical conductivity. Elbaz and co-workers[139] combined the advantages of the FeN$_4$ sites in iron porphyrin and a 3D network of covalent organic framework and carbon aerogel, which managed to achieve a high PEMFC performance with P_{max} of 292 mW cm^{-2} (Fig. 10c) due to the increased surface area and high density of FeN$_4$ sites. The
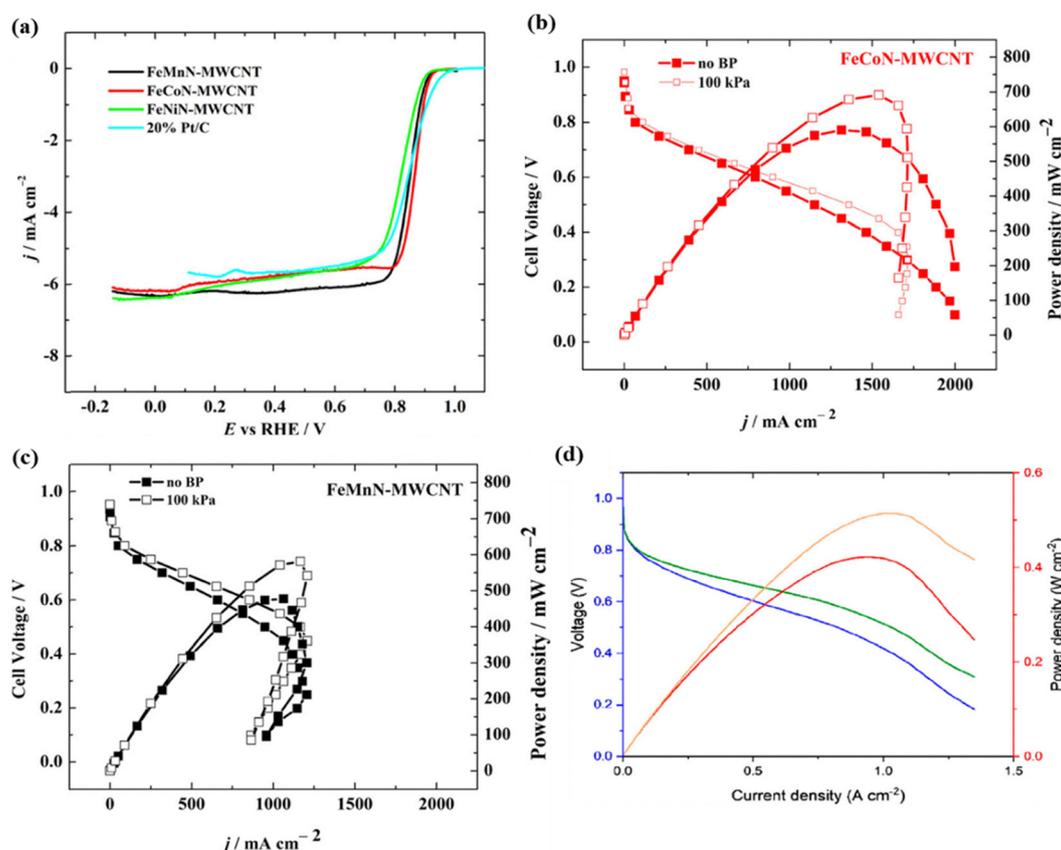

Fig. 9 (a) ORR polarization curves recorded in O$_2$-saturated 0.1 M KOH. AEMFC polarization and power density curves using (b) FeCoN-MWCNT and (c) FeMnN-MWCNT cathode catalysts. Reproduced from ref. 66 under a Creative Commons Attribution Licence (CC-BY), copyright 2021 the authors. (d) AEMFC performance using the HT-FeCu porphyrrole aerogel-based cathode catalyst. Testing conditions: temperature 75/77/80 °C, H$_2$/O$_2$, 150 sccm. Performances with (green and orange) and without (blue and red) iR correction. Reproduced from ref. 137 under a Creative Commons Attribution Licence (CC-BY), copyright 2023 the authors.
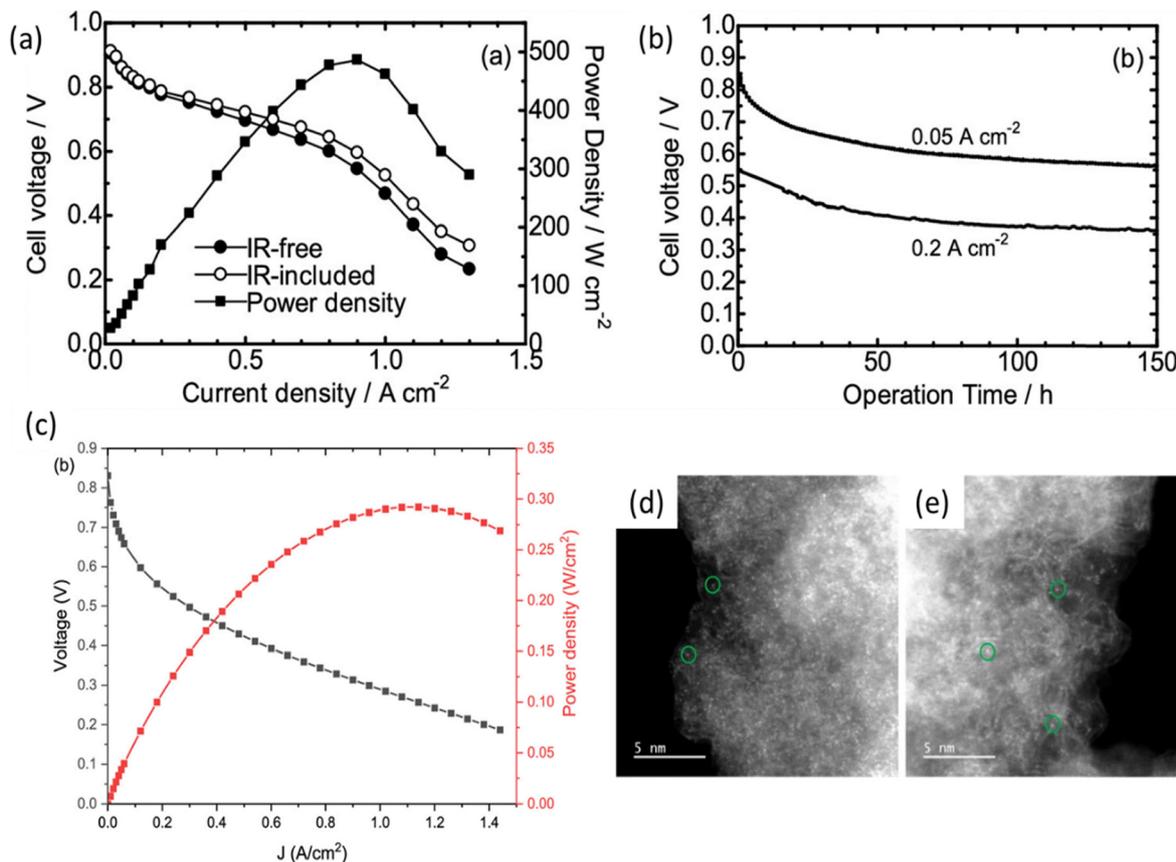
Fig. 10 (a) Polarization and power density curves, and (b) changes in the cell voltage during continuous operation with air at 0.2 and 0.05 A cm^{-2} in the PEMFC testing of Fe14-MR/FePI. Reproduced from ref. 126 under a Creative Commons Attribution Licence (CC-BY), copyright 2025 the authors. (c) H$_2$–O$_2$ PEMFC performance of the Fe800TEPc aerogel, (d and e) ADF-STEM images of the pristine FeTEPc aerogel and heat-treated (at 800 °C) Fe800TEPc aerogel (the green circles show examples of atomically dispersed iron within the aerogel samples). Reproduced from ref. 139 with the permission from the American Chemical Society, copyright 2022.

dispersion of the Fe atoms before and after the heat-treatment was demonstrated through the ADF-STEM images of the pristine FeTEPc aerogel (Fig. 10d) and the heat-treated Fe800TEPc aerogel (Fig. 10e). In order to design high-performing catalysts and understand the nature of active sites in M–N–C type catalysts, it is important to expand understanding of how the density and location of heteroatoms and MN$_x$ sites and pyrolysis temperature directly affect the electrocatalytic ORR behavior of the M–N–C materials. This could involve high-temperature pyrolysis of different precursors in a controlled manner to interpret the formation of active sites, as well as prevent the agglomeration of FeN$_x$ centers during the annealing process. Qu et al.[123] utilized a stepwise pyrolysis strategy to construct atomically dispersed FeN$_x$ sites on a highly graphitized carbon support, resulting in significantly enhanced electrochemical stability in acid media and a high-power density and stability in PEMFC testing conditions.

Non-traditional heat-treatment methods such as microwave-based methods, have also been explored to synthesize M–N–C catalysts, which have shown some success. For example, Ma et al.[121] prepared carbon-supported CoTMPP electrocatalysts by applying the microwave method and reported decent power

density and stability under fuel cell operation at a current density of 200 mA cm^{-2} for 15 h operation. Low-temperature synthesis has attracted wide attention to enhance stability and ORR activity as this method can retain the well-defined chemical structures of the MN$_4$ macrocyclic compounds. This method offers a uniform distribution of MN$_4$ sites on carbon nanosheets. However, these composite catalysts could have durability problems because of their dissolution/dispersion into the acidic or alkaline electrolytes. Alternatively, MN$_x$ macrocyclic covalent organic polymers are mostly fabricated by networking the MN$_x$ macrocyclic monomers with inorganic and/or organic linking. In addition, this would also reduce the density of the MN$_x$ active sites in the catalyst materials. Zhang et al.[140] reported a facile linker-free formation of the FePc conjugate structure by one-pot microwave heating. They employed in situ polymerization of FePc on carbon scaffolds to enhance π–π stacking, which strengthens the interaction between FePc and the carbon support by increasing the delocalization of π electrons. Moreover, the use of advanced methods has allowed a better understanding of M–N–C catalysts, and significant progress can be seen in the field of fuel cell research and development.

4. Summary and prospects

Despite all these advances in the field of MN_4 macrocycle-derived non-precious metal catalysts for AEMFCs and PEMFCs, more efforts are needed to develop a strategy that maximizes their active site utilization. Additionally, the degradation of carbon supports brings the loss of FeN_x sites. Therefore, studying and optimizing the degree of graphitization can effectively restrain the corrosion of the carbon material, and combining this with computational studies can provide stability descriptors for M–N–C catalysts that can enhance their electrocatalytic performance. Apart from this, less emphasis has been given to *ex situ* and *in situ* electrochemical methods for active site quantification in the majority of Fe–N–C catalyst reports. This would enable comparison of turnover frequencies (TOFs) and the formation of activity descriptors among reported catalysts.[28,82] Additionally, the involvement of operando studies in Fe–N–C catalyzed electrocatalytic reactions could provide key insights into active site degradation mechanisms. Research efforts should also be focused on exploring more sustainable precursors, such as biomass-based materials, as well as environmentally friendly and cost-effective synthesis routes, such as non-pyrolyzed methods. Lastly, the synthesis methods should also focus on scalability parameters while also attaining state-of-the-art performance with minimal steps and negative environmental impact, thereby opening significant avenues for the development of cost-effective electrocatalysts for sluggish ORRs in polymer electrolyte fuel cells.

Conflicts of interest

There are no conflicts to declare.

Data availability

No new primary research data were generated or included as part of this review article.

Acknowledgements

Notes and references

1 Md. M. Hossen, Md. S. Hasan, Md. R. I. Sardar, J. B. Haider, Mottakin, K. Tammeveski and P. Atanassov, *Appl. Catal., B*, 2023, **325**, 121733.
2 A. Sarapuu, J. Lilloja, S. Akula, J. H. Zagal, S. Specchia and K. Tammeveski, *ChemCatChem*, 2023, **15**, e202300849.
3 H. A. Firouzjaie and W. E. Mustain, *ACS Catal.*, 2020, **10**, 225–234.
4 X. Ge, A. Sumboja, D. Wuu, T. An, B. Li, F. W. T. Goh, T. S. A. Hor, Y. Zong and Z. Liu, *ACS Catal.*, 2015, **5**, 4643–4667.
5 T. Mo, C. M. Zalitis, C. Jackson, E. Petrucco, J. Sharman and A. R. J. Kucernak, *ACS Catal.*, 2026, **16**(5), 4266–4289.
6 W. E. Mustain, M. Chatenet, M. Page and Y. S. Kim, *Energy Environ. Sci.*, 2020, **13**, 2805–2838.
7 S. Zhang, Y. Sheng, J. Fang, W. Zhu and Z. Zhuang, *Nano Res.*, 2025, **18**, 94907340.
8 H.-J. Choi, N. Ashok Kumar and J.-B. Baek, *Nanoscale*, 2015, **7**, 6991–6998.
9 T. Marshall-Roth, N. J. Libretto, A. T. Wrobel, K. J. Anderton, M. L. Pegis, N. D. Ricke, T. V. Voorhis, J. T. Miller and Y. Surendranath, *Nat. Commun.*, 2020, **11**, 5283.
10 J. Govan, W. Orellana, J. H. Zagal and F. Tasca, *J. Solid State Electrochem.*, 2021, **25**, 15–31.
11 Ed J. H. Zagal and F. Bedioui, *Electrochemistry of N4 Macrocyclic Metal Complexes*, Springer International Publishing, Cham, 2016.
12 Z. Tian, Y. Wang, Y. Li, G. Yao, Q. Zhang and L. Chen, *iScience*, 2022, **25**, 104557.
13 K. Vignarooban, J. Lin, A. Arvay, S. Kolli, I. Kruusenberg, K. Tammeveski, L. Munukutla and A. M. Kannan, *Chin. J. Catal.*, 2015, **36**, 458–472.
14 T. Sun, Q. Wu, R. Che, Y. Bu, Y. Jiang, Y. Li, L. Yang, X. Wang and Z. Hu, *ACS Catal.*, 2015, **5**, 1857–1862.
15 Q. Zhao, Q. Zhang, Y. Wu, Z. Xiao, Y. Peng, Y. Zhou, W. Zhang, H. Lei and R. Cao, *Mater. Today Catal.*, 2024, **5**, 100050.
16 Z. Feng, S. Honda, J. Ohyama, Y. Iwata, K. Awaya, H. Yoshida, M. Machida, K. Higashi, T. Uruga, N. Kawamura, R. Goto, T. Ichihara, R. Kojima, M. Moriya, H. Notsu, S. Nagata, M. Miyoshi, T. Hayakawa and Y. Nabae, *ACS Catal.*, 2024, **14**, 7416–7425.
17 M. Moriya, R. Takahama, K. Kamoi, J. Ohyama, S. Kawashima, R. Kojima, M. Okada, T. Hayakawa and Y. Nabae, *J. Phys. Chem. C*, 2020, **124**, 20730–20735.
18 J. Hyun and H.-T. Kim, *Energy Environ. Sci.*, 2023, **16**, 5633–5662.
19 H. Lei, X. Yang, Z. Chen, D. Rawach, L. Du, Z. Liang, D. Li, G. Zhang, A. C. Tavares and S. Sun, *Adv. Mater.*, 2025, **37**, 2410106.
20 A. Sarapuu, E. Kibena-Põldsepp, M. Borghei and K. Tammeveski, *J. Mater. Chem. A*, 2018, **6**, 776–804.
21 M. Shao, Q. Chang, J.-P. Dodelet and R. Chenitz, *Chem. Rev.*, 2016, **116**, 3594–3657.
22 H. Lei, J. Han, Q. Zhao, J. Liu, L. Yan, W. Zhang and R. Cao, *Chem. Soc. Rev.*, 2025, **54**, 11488–11544.
23 Y. Wang, Y. Pan, X. Zhang, S. Tang, X. Huang, T. Li, R. Cao, J. Zeng, X. Duan and Z. Liu, *Coord. Chem. Rev.*, 2026, **548**, 217233.
24 Y. Lu, W. Li, Y. Fan, L. Cheng, Y. Tang and H. Sun, *Small*, 2024, **20**, 2406180.
25 X. Wang, S. Sun, J. Yao, H. Wan, R. Ma and W. Ma, *Energy Environ. Mater.*, 2024, **7**, e12709.
26 A. Kumar, G. Zhang, W. Liu and X. Sun, *J. Electroanal. Chem.*, 2022, **922**, 116799.
27 L. Scarpetta-Pizo, I. Ponce, R. Oñate, S. Del Valle, Z. Ahmed, K. Tammeveski and J. H. Zagal, *J. Porphyrins Phthalocyanines*, 2025, **29**, 304–321.
28 J. H. Zagal, S. Specchia and P. Atanassov, *Curr. Opin. Electrochem.*, 2021, **27**, 100683.
29 J. Masa, K. Ozoemena, W. Schuhmann and J. H. Zagal, *J. Porphyrins Phthalocyanines*, 2012, **16**, 761–784.
30 S. Yamazaki, *Coord. Chem. Rev.*, 2018, **373**, 148–166.
31 Y. Liu, X. Yue, K. Li, J. Qiao, D. P. Wilkinson and J. Zhang, *Coord. Chem. Rev.*, 2016, **315**, 153–177.
32 K. Tammeveski and J. H. Zagal, *Curr. Opin. Electrochem.*, 2018, **9**, 207–213.
33 J. Yang, J. Tao, T. Isomura, H. Yanagi, I. Moriguchi and N. Nakashima, *Carbon*, 2019, **145**, 565–571.
34 M. P. Oyarzún, N. Silva, D. Cortés-Arriagada, J. F. Silva, I. O. Ponce, M. Flores, K. Tammeveski, D. Bélanger, A. Zitolo, F. Jaouen and J. H. Zagal, *Electrochim. Acta*, 2021, **398**, 139263.
35 A. Kumar, J. M. Gonçalves, J. Lüder, M. Nakamura, L. Angnes, M. Bouvet, M. Bertotti and K. Araki, *Electrochim. Acta*, 2022, **419**, 140397.
36 Z. Yang, Y. Chen, S. Zhang and J. Zhang, *Adv. Funct. Mater.*, 2023, **33**, 2215185.
37 I. Kruusenberg, J. Mondal, L. Matisen, V. Sammelselg and K. Tammeveski, *Electrochem. Commun.*, 2013, **33**, 18–22.
38 K.-M. Zhao, D.-X. Wu, W.-K. Wu, J.-B. Nie, F.-S. Geng, G. Li, H.-Y. Shi, S.-C. Huang, H. Huang, J. Zhang, Z.-Y. Zhou, Y.-C. Wang and S.-G. Sun, *Nat. Catal.*, 2025, **8**, 422–435.

39 A. Kumar, G. Yasin, S. Ajmal, S. Ali, M. A. Mushtaq, M. M. Makhlouf, T. A. Nguyen, P. Bocchetta, R. K. Gupta and S. Ibraheem, *Int. J. Hydrogen Energy*, 2022, **47**, 17621–17629.

40 H. C. Honig and L. Elbaz, *ChemElectroChem*, 2023, **10**, e202300042.

41 L. Wan, K. Zhao, Y.-C. Wang, N. Wei, P. Zhang, J. Yuan, Z. Zhou and S.-G. Sun, *ACS Catal.*, 2022, **12**, 11097–11107.

42 R. Jasinski, *Nature*, 1964, **201**, 1212–1213.

43 H. Jahnke, M. Schönborn and G. Zimmermann, in *Physical and Chemical Applications of Dyestuffs*, ed F. P. Schäfer, H. Gerischer, F. Willig, H. Meier, H. Jahnke, M. Schönborn and G. Zimmermann, Springer-Verlag, Berlin/Heidelberg, 1976, vol. 61, pp. 133–181.

44 V. S. Bagotzky, M. R. Tarasevich, K. A. Radyushkina, O. A. Levina and S. I. Andrusyova, *J. Power Sources*, 1978, **2**, 233–240.

45 S. Yang, Y. Yu, X. Gao, Z. Zhang and F. Wang, *Chem. Soc. Rev.*, 2021, **50**, 12985–13011.

46 E. Luo, Y. Chu, J. Liu, Z. Shi, S. Zhu, L. Gong, J. Ge, C. H. Choi, C. Liu and W. Xing, *Energy Environ. Sci.*, 2021, **14**, 2158–2185.

47 S. Aralekallu and V. Singh, *Fuel*, 2026, **404**, 136163.

48 X. Jin, J. Fu, C. Zhao, M. Liu, Y. Xie, Y.-M. Kang and J. Zhang, *J. Electroanal. Chem.*, 2024, **967**, 118398.

49 Z. Zhai, Y. Lv, C. Qiu, R. Zheng, J. Li, A. Wang and Y. Song, *J. Electrochem. Soc.*, 2019, **166**, F441–F447.

50 Y. Hong, L. Li, B. Huang, X. Tang, W. Zhai, T. Hu, K. Yuan and Y. Chen, *Adv. Energy Mater.*, 2021, **11**, 2100866.

51 Z. Zhai, Q. Liu, R. Zheng, C. Qiu, J. Qin, J. Li, Y. Xie, A. Wang, J. Huang and Y. Song, *Int. J. Hydrogen Energy*, 2021, **46**, 11041–11050.

52 R. Praats, I. Kruusenberg, M. Käärik, U. Joost, J. Aruväli, P. Paiste, R. Saar, P. Rauwel, M. Kook, J. Leis, J. H. Zagal and K. Tammeveski, *Electrochim. Acta*, 2019, **299**, 999–1010.

53 C. Domínguez, M. A. Peña, S. Rojas and F. J. Pérez-Alonso, *Int. J. Hydrogen Energy*, 2016, **41**, 22560–22569.

54 M. Mooste, T. Tkesheliadze, J. Kozlova, A. Kikas, V. Kisand, A. Treshchalov, A. Tamm, J. Aruväli, J. H. Zagal, A. M. Kannan and K. Tammeveski, *Int. J. Hydrogen Energy*, 2021, **46**, 4365–4377.

55 R.-M. Sun, Y.-Q. Yao, A.-J. Wang, K.-M. Fang, L. Zhang and J.-J. Feng, *J. Colloid Interface Sci.*, 2021, **592**, 405–415.

56 Z. Jin, Y. Chen, J. Sun, S. Zhang and J. Zhang, *Mater. Sci. Eng. R Rep.*, 2025, **165**, 101027.

57 F. Charreteur, F. Jaouen and J.-P. Dodelet, *Electrochim. Acta*, 2009, **54**, 6622–6630.

58 H. Meng, N. Larouche, M. Lefèvre, F. Jaouen, B. Stansfield and J.-P. Dodelet, *Electrochim. Acta*, 2010, **55**, 6450–6461.

59 F. Roncaroli, E. S. Dal Molin, F. A. Viva, M. M. Bruno and E. B. Halac, *Electrochim. Acta*, 2015, **174**, 66–77.

60 I. Kruusenberg, L. Matisen and K. Tammeveski, *Int. J. Electrochem. Sci.*, 2013, **8**, 1057–1066.

61 I. Kruusenberg, L. Matisen and K. Tammeveski, *J. Nanosci. Nanotechnol.*, 2013, **13**, 621–627.

62 M. Muhyuddin, E. Berretti, S. A. Mirshokraee, J. Orsilli, R. Lorenzi, L. Capozzoli, F. D'Acapito, E. Murphy, S. Guo, P. Atanassov, A. Lavacchi and C. Santoro, *Appl. Catal., B*, 2024, **343**, 123515.

63 C. H. Choi, H.-K. Lim, M. W. Chung, G. Chon, N. Ranjbar Sahraie, A. Altin, M.-T. Sougrati, L. Stievano, H. S. Oh, E. S. Park, F. Luo, P. Strasser, G. Dražić, K. J. J. Mayrhofer, H. Kim and F. Jaouen, *Energy Environ. Sci.*, 2018, **11**, 3176–3182.

64 Z. Zhang, M. Dou, H. Liu, L. Dai and F. Wang, *Small*, 2016, **12**, 4193–4199.

65 R. Jiang and D. Chu, *J. Power Sources*, 2014, **245**, 352–361.

66 Y. Kumar, E. Kibena-Põldsepp, J. Kozlova, M. Rähn, A. Treshchalov, A. Kikas, V. Kisand, J. Aruväli, A. Tamm, J. C. Douglin, S. J. Folkman, I. Gelmetti, F. A. Garcés-Pineda, J. R. Galán-Mascarós, D. R. Dekel and K. Tammeveski, *ACS Appl. Mater. Interfaces*, 2021, **13**, 41507–41516.

67 S. A. Mirshokraee, M. Muhyuddin, N. Pianta, E. Berretti, L. Capozzoli, J. Orsilli, F. D'Acapito, R. Viscardi, A. Cosenza, P. Atanassov, C. Santoro and A. Lavacchi, *ACS Catal.*, 2024, **14**, 14524–14538.

68 M. Ladouceur, G. Lalande, D. Guay, J. P. Dodelet, L. Dignard-Bailey, M. L. Trudeau and R. Schulz, *J. Electrochem. Soc.*, 1993, **140**, 1974–1981.

69 J. M. Ziegelbauer, T. S. Olson, S. Pylypenko, F. Alamgir, C. Jaye, P. Atanassov and S. Mukerjee, *J. Phys. Chem. C*, 2008, **112**, 8839–8849.

70 S. A. Mirshokraee, M. Muhyuddin, J. Orsilli, E. Berretti, A. Lavacchi, C. Lo Vecchio, V. Baglio, R. Viscardi, A. Zaffora, F. Di Franco, M. Santamaria, L. Olivi, S. Pollastri and C. Santoro, *Nanoscale*, 2024, **16**, 6531–6547.

71 K.-K. Türk, I. Kruusenberg, J. Mondal, P. Rauwel, J. Kozlova, L. Matisen, V. Sammelselg and K. Tammeveski, *J. Electroanal. Chem.*, 2015, **756**, 69–76.

72 Y. Pan, S. Liu, K. Sun, X. Chen, B. Wang, K. Wu, X. Cao, W. Cheong, R. Shen, A. Han, Z. Chen, L. Zheng, J. Luo, Y. Lin, Y. Liu, D. Wang, Q. Peng, Q. Zhang, C. Chen and Y. Li, *Angew. Chem., Int. Ed.*, 2018, **57**, 8614–8618.

73 W. Orellana, C. Z. Loyola, J. F. Marco and F. Tasca, *Sci. Rep.*, 2022, **12**, 8072.

74 Z. Yang, Q. Wu, H. Zhang, C. Hu, X. Bao and P. Yuan, *ChemSusChem*, 2025, **18**, e202500855.

75 D. Liu, X. Wan and J. Shui, *Small*, 2024, **20**, 2406078.

76 Q. Ye, H. Yu, S. Wang, H. Zhuo, W. Li, T. Jin, L. Feng, Z. Fu, Z. Liu, H. Liu and W. Chen, *ACS Appl. Polym. Mater.*, 2025, **7**, 5979–5992.

77 J. H. Zagal, I. Ponce, D. Baez, R. Venegas, J. Pavez, M. Paez and M. Gulppi, *Electrochem. Solid-State Lett.*, 2012, **15**, B90.

78 A. Alsudairi, J. Li, N. Ramaswamy, S. Mukerjee, K. M. Abraham and Q. Jia, *J. Phys. Chem. Lett.*, 2017, **8**, 2881–2886.

79 N. Ramaswamy, U. Tylus, Q. Jia and S. Mukerjee, *J. Am. Chem. Soc.*, 2013, **135**, 15443–15449.

80 J. H. Zagal and M. T. M. Koper, *Angew. Chem., Int. Ed.*, 2016, **55**, 14510–14521.

81 J. H. Zagal, F. Javier Recio, C. A. Gutierrez, C. Zuñiga, M. A. Páez and C. A. Caro, *Electrochem. Commun.*, 2014, **41**, 24–26.

82 S. Specchia, P. Atanassov and J. H. Zagal, *Curr. Opin. Electrochem.*, 2021, **27**, 100687.

83 L. Scarpetta-Pizo, L. Acuña-Saavedra, I. Ponce and J. H. Zagal, *Curr. Opin. Electrochem.*, 2026, **55**, 101779.

84 L. Acuña-Saavedra, A. M. Méndez-Torres, G. Cárdenas-Jirón, R. Oñate, B. Sánchez-Allende, R. Venegas, R. Bernal, F. Melo, E. Imbarack, J. H. Zagal and I. Ponce, *ACS Catal.*, 2025, **15**, 719–737.

85 L. Scarpetta-Pizo, R. Venegas, K. Muñoz-Becerra, L. Muñoz, A. Toro-Labbé, N. Darwish, R. Matute, R. Oñate, J. H. Zagal and I. Ponce, *Electrochim. Acta*, 2023, **468**, 143160.

86 K.-Z. Yang, C. Xu, P.-P. Guo, Y.-M. Zhao, H.-M. Chi, Y. Xu, P.-J. Wei, T. Zheng, Q. He, Q. Ren and J.-G. Liu, *ACS Sustainable Chem. Eng.*, 2024, **12**, 11033–11043.

87 C. Zúñiga, C. Candia-Onfray, R. Venegas, K. Muñoz, J. Urra, M. Sánchez-Arenillas, J. F. Marco, J. H. Zagal and F. J. Recio, *Electrochem. Commun.*, 2019, **102**, 78–82.

88 S. Yuan, J. Peng, Y. Zhang, D. J. Zheng, S. Bagi, T. Wang, Y. Román-Leshkov and Y. Shao-Horn, *ACS Catal.*, 2022, **12**, 7278–7287.

89 R. Venegas, K. Muñoz-Becerra, C. Candia-Onfray, J. F. Marco, J. H. Zagal and F. J. Recio, *Electrochim. Acta*, 2020, **332**, 135340.

90 A. Kumar, Y. Zhang, W. Liu and X. Sun, *Coord. Chem. Rev.*, 2020, **402**, 213047.

91 C. Domínguez, F. J. Pérez-Alonso, M. Abdel Salam, J. L. Gómez De La Fuente, S. A. Al-Thabaiti, S. N. Basahel, M. A. Peña, J. L. G. Fierro and S. Rojas, *Int. J. Hydrogen Energy*, 2014, **39**, 5309–5318.

92 N. Giulini, M. Muhyuddin, S. Mattiello, M. Sassi, C. Lo Vecchio, V. Baglio, E. Berretti, A. Lavacchi, E. Fazio, L. Beverina and C. Santoro, *Electrochim. Acta*, 2024, **507**, 145113.

93 C. Ling, W.-Y. Xie, S.-F. He, G.-C. Liang, S.-Y. Xiao, C.-L. Yang and H.-Y. Liu, *J. Alloys Compd.*, 2024, **987**, 174172.

94 K. Fang, C. Ling, Y.-F. Yao, H. Zhang, J.-J. Wu, L.-P. Si and H.-Y. Liu, *J. Environ. Chem. Eng.*, 2025, **13**, 116391.

95 C. Ling, K. Fang, Y.-R. Lv, S.-F. He, G. Liang, X.-Y. Xiao and H.-Y. Liu, *Int. J. Hydrogen Energy*, 2025, **123**, 194–208.

96 Y. Jiang, Y. Xie, X. Jin, Q. Hu, L. Chen, L. Xu and J. Huang, *RSC Adv.*, 2016, **6**, 78737–78742.

97 X. Jin, Y. Xie and J. Huang, *Catalysts*, 2017, **7**, 201.

98 X.-S. Guo, Z.-Y. Huang, X.-W. Qi, L.-P. Si, H. Zhang and H.-Y. Liu, *J. Electroanal. Chem.*, 2023, **936**, 117381.

99 S. Tian, S. Wu, J. Yang, J. Li, C. Liu, J. Shi, X. Xiang, L. Wang, Y. Sun and Q. Yang, *J. Electroanal. Chem.*, 2025, **980**, 118991.

100 L. Jiao, G. Wan, R. Zhang, H. Zhou, S. Yu and H. Jiang, *Angew. Chem., Int. Ed.*, 2018, **57**, 8525–8529.

101 Y. Sun, K. Xiong, G. Zhang, K. Cheng, S. Feng, H. Chen, M. Li, K. Chen, Y. Chen, H. Jin and S. Wang, *Chem. Eng. J.*, 2025, **519**, 165652.

102 Y. Chen, X. Hua and S. Chen, *Chin. J. Catal.*, 2016, **37**, 1166–1171.
103 D. Banham, S. Ye, K. Pei, J. Ozaki, T. Kishimoto and Y. Imashiro, *J. Power Sources*, 2015, **285**, 334–348.
104 Z. Feng, J. Ohyama, S. Honda, Y. Iwata, K. Awaya, M. Machida, M. Tsushida, R. Goto, T. Ichihara, M. Moriya and Y. Nabae, *J. Am. Chem. Soc.*, 2025, **147**, 15377–15388.
105 K. Jong Gyeong, C. Youngin and P. Chanho, *J. Electrochem. Sci. Technol.*, 2024, **15**, 207–219.
106 D. Y. Chung, M. J. Kim, N. Kang, J. M. Yoo, H. Shin, O.-H. Kim and Y.-E. Sung, *Chem. Mater.*, 2017, **29**, 2890–2898.
107 L. Zhang, D. P. Wilkinson, Y. Liu and J. Zhang, *Electrochim. Acta*, 2018, **262**, 326–336.
108 K. Muuli, A. Sokka, M. Mooste, J. Lilloja, V. Gudkova, M. Käärik, M. Otsus, A. Kikas, V. Kisand, A. Tamm, J. Leis, A. Krumme, S. Holdcroft, J. H. Zagal and K. Tammeveski, *J. Catal.*, 2023, **422**, 117–130.
109 Z. Chen, S. M. Zahan and D. R. Dekel, *ACS Catal.*, 2026, **16**, 992–1001.
110 Y. Kumar, E. Kibena-Põldsepp, M. Mooste, J. Kozlova, A. Kikas, J. Aruväli, M. Käärik, V. Kisand, J. Leis, A. Tamm, S. Holdcroft, J. H. Zagal and K. Tammeveski, *ChemElectroChem*, 2022, **9**, e202200717.
111 Y. J. Sa, D.-J. Seo, J. Woo, J. T. Lim, J. Y. Cheon, S. Y. Yang, J. M. Lee, D. Kang, T. J. Shin, H. S. Shin, H. Y. Jeong, C. S. Kim, M. G. Kim, T.-Y. Kim and S. H. Joo, *J. Am. Chem. Soc.*, 2016, **138**, 15046–15056.
112 H. A. Miller, M. Bellini, W. Oberhauser, X. Deng, H. Chen, Q. He, M. Passaponti, M. Innocenti, R. Yang, F. Sun, Z. Jiang and F. Vizza, *Phys. Chem. Chem. Phys.*, 2016, **18**, 33142–33151.
113 J. Guo, H. He, D. Chu and R. Chen, *Electrocatalysis*, 2012, **3**, 252–264.
114 J. Woo, S. Y. Yang, Y. J. Sa, W.-Y. Choi, M.-H. Lee, H.-W. Lee, T. J. Shin, T.-Y. Kim and S. H. Joo, *Chem. Mater.*, 2018, **30**, 6684–6701.
115 Z. Ahmed, S. Akula, J. Kozlova, H.-M. Piirsoo, K. Kukli, A. Kikas, V. Kisand, M. Käärik, J. Leis, A. Treshchalov, J. Aruväli and K. Tammeveski, *Int. J. Hydrogen Energy*, 2024, **62**, 849–858.
116 R. Praats, M. Käärik, A. Kikas, V. Kisand, J. Aruväli, P. Paiste, M. Merisalu, A. Sarapuu, J. Leis, V. Sammelselg, J. C. Douglin, D. R. Dekel and K. Tammeveski, *J. Solid State Electrochem.*, 2021, **25**, 57–71.
117 R. Praats, M. Käärik, A. Kikas, V. Kisand, J. Aruväli, P. Paiste, M. Merisalu, J. Leis, V. Sammelselg, J. H. Zagal, S. Holdcroft, N. Nakashima and K. Tammeveski, *Electrochim. Acta*, 2020, **334**, 135575.
118 I. Kruusenberg, L. Matisen, Q. Shah, A. M. Kannan and K. Tammeveski, *Int. J. Hydrogen Energy*, 2012, **37**, 4406–4412.
119 N. Zion, J. C. Douglin, D. A. Cullen, P. Zelenay, D. R. Dekel and L. Elbaz, *Adv. Funct. Mater.*, 2021, **31**, 2100963.
120 Y. Nabae, M. Sonoda, C. Yamauchi, Y. Hosaka, A. Isoda and T. Aoki, *Catal. Sci. Technol.*, 2014, **4**, 1400–1406.
121 Z.-F. Ma, X.-Y. Xie, X.-X. Ma, D.-Y. Zhang, Q. Ren, N. Heß-Mohr and V. M. Schmidt, *Electrochem. Commun.*, 2006, **8**, 389–394.
122 L. Yang, N. Larouche, R. Chenitz, G. Zhang, M. Lefèvre and J.-P. Dodelet, *Electrochim. Acta*, 2015, **159**, 184–197.
123 X. Qu, Y. Han, Y. Chen, J. Lin, G. Li, J. Yang, Y. Jiang and S. Sun, *Appl. Catal., B*, 2021, **295**, 120311.
124 X. Li, Q. Liu, B. Yang, Z. Liao, W. Yan and Z. Xiang, *Adv. Mater.*, 2022, **34**, 2204570.
125 M. Muhyuddin, A. Friedman, F. Poli, E. Petri, H. Honig, F. Basile, A. Fasolini, R. Lorenzi, E. Berretti, M. Bellini, A. Lavacchi, L. Elbaz, C. Santoro and F. Soavi, *J. Power Sources*, 2023, **556**, 232416.
126 Y. Nabae, Y. Tao, S. Nagata, H. Notsu, M. Miyoshi, K. Hatakeyama-Sato, T. Hayakawa, M. Moriya, Z. Feng and J. Ohyama, *ACS Appl. Nano Mater.*, 2025, **8**, 8740–8750.
127 G. Zuccante, M. Acciarri, C. L. Vecchio, I. Gatto, V. Baglio, N. Pianta, R. Ruffo, L. Navarini and C. Santoro, *Electrochim. Acta*, 2024, **492**, 144353.
128 J. Li, L. Wang, Y. Fu, K. Qian, Q. Shi, Q. Liu, R. Yu, W. Yang, H. Shu and Q. Wei, *ACS Appl. Energy Mater.*, 2025, **8**, 552–558.
129 H. C. Honig, S. Mostoni, Y. Presman, R. Z. Snitkoff-Sol, P. Valagussa, M. D'Arienzo, R. Scotti, C. Santoro, M. Muhyuddin and L. Elbaz, *Nanoscale*, 2024, **16**, 11174–11186.
130 I. Jang, S. Lee, D. Kim, V. K. Paidi, S. Lee, N. D. Kim, J. Y. Jung, K. Lee, H. Lim, P. Kim and S. J. Yoo, *Adv. Mater.*, 2024, **36**, 2403273.
131 T. Zhu, X. Qing, P. Xu, Y. Song and J. Qiao, *ECS Trans.*, 2015, **66**, 105–110.
132 G. Abarca, M. Viera, C. Aliaga, J. F. Marco, W. Orellana, J. H. Zagal and F. Tasca, *J. Mater. Chem. A*, 2019, **7**, 24776–24783.
133 A. Friedman, M. Mizrahi, N. Levy, N. Zion, M. Zachman and L. Elbaz, *ACS Appl. Mater. Interfaces*, 2021, **13**, 58532–58538.
134 K.-Z. Yang, Y.-Z. Su, C. Xu, P.-P. Guo, Y.-M. Zhao, X. Liu, L. Jia, Y. Yang, H.-N. Zhu, P.-J. Wei and J.-G. Liu, *ACS Catal.*, 2025, **15**, 8114–8124.
135 R. Ren, X. Wang, H. Chen, H. A. Miller, I. Salam, J. R. Varcoe, L. Wu, Y. Chen, H. Liao, E. Liu, F. Bartoli, F. Vizza, Q. Jia and Q. He, *Angew. Chem., Int. Ed.*, 2021, **60**, 4049–4054.
136 S. S. Chougule, A. A. Jeffery, D. Kim, M. Kim, Y. Kim, K. Ko, J. Min, K. Davletbaev, A. A. Chavan, H. Park, Y. Lee, S. Jang and N. Jung, *J. Am. Ceram. Soc.*, 2025, **108**, e20557.
137 Y. Persky, Ł. Kielesiński, S. N. Reddy, N. Zion, A. Friedman, H. C. Honig, B. Koszarna, M. J. Zachman, I. Grinberg, D. T. Gryko and L. Elbaz, *ACS Catal.*, 2023, **13**, 11012–11022.
138 Y. Persky, Y. Yurko, R. Z. Snitkoff-Sol, N. Zion and L. Elbaz, *Nanoscale*, 2024, **16**, 438–446.
139 N. Zion, L. Peles-Strahl, A. Friedman, D. A. Cullen and L. Elbaz, *ACS Appl. Energy Mater.*, 2022, **5**, 7997–8003.
140 H. Zhang, S. Zhang, Y. Wang, J. Si, Y. Chen, L. Zhuang and S. Chen, *ACS Appl. Mater. Interfaces*, 2018, **10**, 28664–28671.